

VELOCITY MEASUREMENTS AND CFD PREDICTIONS
OF FLOW REDISTRIBUTION THROUGH
AIR FILTERS

By

GUOJIANG LIU

of

Philosophy of Science

Norwegian Institute of Technology

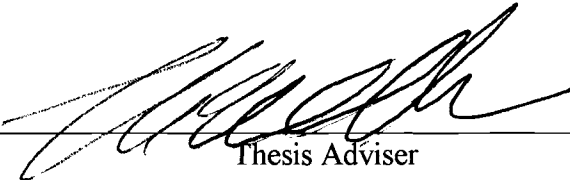
Trondheim, Norway

1994

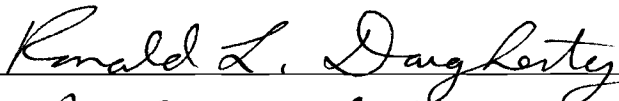
Submitted to the Faculty of the
Graduate College of the
Oklahoma State University
in partial fulfillment of
the requirements for
the Degree of
MASTER OF SCIENCE
December, 1995

VELOCITY MEASUREMENTS AND CFD PREDICTIONS
OF FLOW REDISTRIBUTION THROUGH
AIR FILTERS

Thesis Approved:



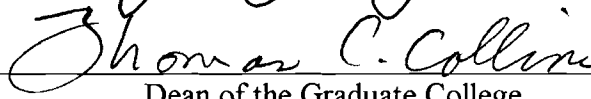
Thesis Adviser



Ronald L. Daugherty



A. J. Yhojan



Thomas C. Collins
Dean of the Graduate College

ACKNOWLEDGMENTS

This thesis would not have been possible without the encouragement, guidance and friendship from numerous people. I am sincerely grateful to my academic supervisor Dr. Frank W. Chambers for accepting me as one of his research assistants. Dr. Chambers has invested a lot of time to help me both in academic and personal matters. I admire Dr. Chambers for his honesty and amicability toward people, and for his profound knowledge of fluid mechanics. I thank Dr. Ronald L. Dougherty for being a committee member of my thesis. Dr. Dougherty has not only offered me a lot of help in my experimental work. The most valuable lesson I have learnt from him is the spirit to search for the truth of sciences with diligence, zeal, and foresight of the future. I thank Dr. A. J. Ghajar for being a committee member of my thesis and for spending time on this thesis.

My colleagues and friends Charles B. Tebbutt, Robert Duran, have provided me a lot of help in my experimental work. My thanks also go to Balu Natarajan for helping me to use some plotting programs. The financial support provided by Purolator Products, Inc. and the Oklahoma Center for the Advancement of Science and Technology (OCAST) is sincerely appreciated.

Finally, I am sincerely grateful to my wife, Wei Song and my son Trond for their love, encouragement and patience with me during the months of hard work to get this thesis done.

TABLE OF CONTENTS

Chapter	Page
1	A GENERAL INTRODUCTION 1
	1.1 Outline of The Thesis 1
	1.2 Summary of Chapter 2 3
	1.3 Summary of Chapter 3 7
2	CFD MODELING OF THE AIR FLOW THROUGH POROUS MEDIA 11
	Abstract 11
	2.1 Introduction 13
	2.2 Partial Differential Equations 22
	2.2.1 <i>Equations for Laminar Flow</i> 22
	2.2.2 <i>Equations for Turbulent Flow</i> 24
	2.3 Finite Difference Equations 28
	2.3.1 <i>Laminar Flow</i> 28
	2.3.2 <i>Turbulent Flow</i> 33
	2.4 Initial and Boundary Conditions 37
	2.5 Solution Procedure and Pressure Iteration 39
	2.6 Numerical Stability Considerations 41
	2.7 Results and Discussion 44
	2.7.1 <i>The Effects of Grid Size and Time</i>
	<i>Step on Velocity Changes</i> 45
	2.7.2 <i>General Characteristics of the Flow</i>
	<i>Fields with Uniform K</i> 48

	2.7.1 <i>The Effects of Grid Size and Time</i>	
	<i>Step on Velocity Changes</i>	45
	2.7.2 <i>General Characteristics of the Flow</i>	
	<i>Fields with Uniform K</i>	48
	2.7.3 <i>Effects of the Inhomogeneity of K</i>	55
	2.7.4 <i>Discussion</i>	62
	2.7.5 <i>Conclusions</i>	64
3	EFFECTS OF THE DUST LOADING ON FILTER INLET	
	VELOCITY REDISTRIBUTION	66
	Abstract	66
	3.1 Introduction	68
	3.2 Dust Loading Experiments	73
	3.3 LDA Velocity Measurements	75
	3.4 Results and Discussion	79
	3.5 Conclusions.....	86
4	FUTURE WORK.....	88
	REFERENCES.....	91
	APPENDIX	95

LIST OF TABLES

Table	Page
2.1 The constants used in the standard k- ϵ model (after Rodi, 1980)	27
2.2 The constants used in this study, where the code names are consistent with those in the program TLUV2D	44
2.3 Velocity changes with time at the geometrical center of the filter with a uniform K of 10^{-4} m^2 and Δt 100 times smaller than the stability criterion.....	47
3.1 Filter specifications and the design flow rate.....	71
3.2 The filter capacities and elapsed dust loading times for various terminating pressure drops	74

LIST OF FIGURES

Figure	Page
2.1 The top and side views of the Purolator AF3192 filter. The pleats are 3 cm high with a 3 mm pitch. The media is about 635 μ m thick.....	16
2.2 The shape of a single pleat in an air filter. (A) is the approximate real form of pleats with each pleat in an elliptical shape. (B) is the pleats used by Cai (1993) with each pleat in a triangular shape.....	16
2.3 A sketch of the computational domain. The shaded area is a porous medium or filter. d is the effective filter thickness.....	18
2.4 A sketch of the discretization of the computational domain into cells.....	29
2.5 A sketch showing the nodes and nodal variable locations for the cell (i,j) (after Hirt et al., 1975).....	29
2.6 The effect of time step on the solution of the axial velocity at the center of the filter with a uniform K and Δx equal to 10^{-4} m^2 and 0.01 m, respectively. The numbers in the legend are Δt in seconds.....	46
2.7 The axial velocity distribution in the computational domain with K and grid size equal to 10^{-4} m^2 and 0.01 m, respectively.....	50
2.8 The velocity field for a uniform K of 10^{-4} m^2 and grid size of 0.01 m.....	51
2.9 Pressure distributions along the center-line of the filter, where K in the legend is the permeability (in m^2).....	52
2.10 A comparison of the axial velocities at x equal to 0.13 m for different permeability, K , in m^2 . The filter is located between x equal to 0.15 and 0.20 m.....	53
2.11 The flow field with K equal to 10^{-6} m^2 and the effective thickness.....	54
2.12 The flow field with K equal to 10^{-8} m^2 at the central strip (0.04 m thick) and 10^{-6} m^2 for the rest of the filter.....	57

2.12	The flow field with K equal to 10^{-8} m^2 at the central strip (0.04 m thick) and 10^{-6} m^2 for the rest of the filter	57
2.13	A comparison of the axial velocities at x equal to 0.15 m. The filter is located between 0.15 and 0.20 m. K equals 10^{-6} m^2 (for Series 1) and 10^{-7} m^2 (for Series 2) outside the core area, and 10^{-8} m^2 at the core area (for both Series 1 and 2).	58
2.14	The velocity field with K equal to 10^{-8} and 10^{-6} m^2 for the left half and right half of the filter, respectively.	59
2.15	The axial velocity distribution at y equal to 0.1 m (the center in the y-direction) with a non-uniform distribution of K in the filter	60
2.16	The distribution of permeability in the filter where the number is the zone number.....	60
2.17	The velocity field with K distribution as shown in Figure 2.16	61
3.1	A sketch of test housing.....	72
3.2	The capacities and elapsed dust loading times for various desired additional pressure drops. The flow and other parameters are listed in Table 3.1. The dimensions of the y-axis are grams and minutes for the capacity and elapsed time curves, respectively.....	74
3.3	The velocity distribution at the plane 12.7 mm upstream of a clean filter with a volumetric air flow rate of $0.059 \text{ m}^3/\text{s}$	80
3.4	The velocity distribution at the plane 12.7 mm upstream of the dirty filter loaded to an additional 127 mm water pressure drop with $0.059 \text{ m}^3/\text{s}$ volumetric air flow rate.....	81
3.5	The velocity distribution at the plane 12.7 mm upstream of the dirty filter loaded to an additional 254 mm water pressure drop with $0.059 \text{ m}^3/\text{s}$ volumetric air flow rate.....	81
3.6	The velocity distribution at the plane 12.7 mm upstream of the dirty filter loaded to an additional 381 mm water pressure drop with a volumetric air flow rate of $0.059 \text{ m}^3/\text{s}$	82
3.7	A comparison of axial velocity at y equal to zero from dirty filters with terminating pressures of 127, 254, and 381 mm of water.....	85

3.8 The transverse velocity distribution at the level of 12.7 mm upstream of a filter loaded to an additional 381 mm water additional pressure drop with 0.059 m³/s volumetric air flow rate..... 85

NOMENCLATURE

b	inertial factor (m^{-1})
$C_{\mu}, C_{1\epsilon}, C_{2\epsilon}$	constants of k- ϵ model
d	effective filter thickness of an air filter (m)
D	mass divergence of continuity equation (1/s)
D_{in}	the diameter of the inlet flow (m)
g_x, g_y	gravitational acceleration in x- and y-direction, respectively (m/s^2)
J	unit vector in extended Darcy's law
k	turbulent kinetic energy (m^2/s^2)
$k_{i,j}$	turbulent kinetic energy at the cell (i, j) (m^2/s^2)
K	permeability of a filter (m^2)
P	pressure N/m^2 .
$P_{i,j}$	pressure at cell (i, j) (N/m^2)
ΔP	pressure change or correction (N/m^2)
$\langle P \rangle^f$	pressure read off a pressure gauge in a pore (N/m^2)
t	time (s)
u	turbulent velocity fluctuation in x-direction (m/s)
$U_{i,j}$	instantaneous velocity in x-direction at the cell (i,j) (m/s)
U_{in}	inlet velocity (m/s)
v	turbulent velocity fluctuation in y-direction (m/s)
$V_{i,j}$	instantaneous velocity in y-direction at the cell (i,j) (m/s)

\bar{U}	turbulent mean velocity component in x-direction (m/s)
\bar{V}	turbulent mean velocity component in y-direction (m/s)
V	velocity vector

Greek Symbols

α	donor cell coefficient
$\delta_{i,j}$	Kronecker delta
ε	turbulent energy dissipation rate (N/(s•m ²))
$\varepsilon_{i,j}$	ε at the cell (i, j) (N/(s•m ²))
ϕ	porosity
μ	fluid dynamic viscosity (N•s/m ²)
μ_t	turbulent dynamic viscosity (N•s/m ²)
ρ	density (kg/m ³)
$\sigma_k, \sigma_\varepsilon$	constants for the standard k- ε model
τ_x, τ_y	turbulent stress
ν_t	eddy viscosity (m ² /s)
ω	over-relaxation factor
$\langle \rangle$	local volume average of a quantity
Ω_x^u, Ω_y^u	convections in the x-momentum equation with respect to x and y, respectively.
Ω_x^v, Ω_y^v	convections in the y-momentum equation. with respect to x and y, respectively.
Γ_u	diffusion in the x-momentum equation
Γ_v	diffusion in the y-momentum equation
Λ_k	production in the k-equation
Λ_ε	production in the ε -equation

Superscript

n denotes the value at current time step t

n+1 denotes the value at advanced time step $t+\Delta t$

Subscript

x horizontal component value

y vertical component value

CHAPTER 1

A GENERAL INTRODUCTION

1.1 OUTLINE OF THE THESIS

To increase dust holding capacity, to enhance filtration efficiency, and to prolong the life span of automotive air filters have long been the major concerns of the automotive filter engineers. Since early this century, numerous experiments on dust loading and velocity measurements have been conducted. The Society of Automotive Engineers (SAE) recognized the need for standardization of these experiments. Therefore, in 1947, a standard air cleaner test code was proposed, the SAE J726 Air Cleaner Test Code, which was last revised in 1987.

Previous flow visualization and Laser Doppler Anemometer (LDA) velocity measurements (Sabnis et al., 1994a, b; Newman, 1994; Duran, 1995) have shown that the velocity distribution upstream of a clean filter is very non-uniform and impinging jet-like when tested under the SAE test housing. The high velocity peak occurs at the center of the filter. Velocities decrease rapidly toward the edges of the filter. This is a very undesired situation, because the very non-uniform velocity upstream of a filter may induce a non-uniform deposition of dust during engine operations (Liang et al., 1994). The preferential deposition of dust will affect the filtration efficiency and endurance of the

a non-uniform deposition of dust during engine operations (Liang et al., 1994). The preferential deposition of dust will affect the filtration efficiency and endurance of the automotive air filters. Duran (1995) conducted experiments using the SAE test housing, attempting to improve the velocity distribution upstream of automotive filters. Duran inserted a sphere at the center of the inlet of the SAE test housing to diverge the impinging jet-like inlet flow. However, Duran's results showed little improvement in the velocity distribution at the level 12.7 mm upstream of a filter (Duran, 1995, p. 94).

Most previously documented experiments were concerned with clean panel air filters. The effects of dust loading on the velocity distribution are not well-known. Dust loading onto an automotive filter will partially block air flow passages and reduce the permeability of the filter, and consequently will affect the velocity distribution upstream of the filter. This can be reasoned from Darcy's law. Because the dust loading onto a filter will locally decrease the permeability of the filter, for a given pressure drop, the velocity will be higher at the area of high permeability. However, to the author's knowledge, the effects of the dust loading on the inlet velocity redistribution have not been documented. Therefore, the present thesis intends to depict the flow field or velocity distribution inside the automotive air induction system through LDA velocity measurements and CFD modeling techniques.

The main theme of the present thesis is the effects of the dust loading, and the accompanying changes in permeability, on the velocity distribution upstream of the panel air filter. The problem will be attacked through two avenues. The first is using LDA velocity measurements of the velocity distribution upstream of both clean and dirty panel

techniques to investigate the velocity distribution inside a simplified two-dimensional air induction system.

This thesis consists of the present introductory chapter and two self-contained papers arranged as Chapter 2 and 3, respectively, and future work arranged as Chapter 4. A general bibliography is provided at the end of the thesis. Chapter 2 deals with the CFD modeling of the fluid flow through porous media and Chapter 3 contains the LDA velocity measurements at 12.7 mm upstream of the clean and dirty automotive panel air filters.

1.2 SUMMARY OF CHAPTER 2

The present study intends to predict the flow field inside an automotive air induction system assuming two-dimensional air flow. The main objective of the present study is, by using the technique of CFD modeling, to understand the flow field inside the automotive air induction system in order to enhance the performance of automotive air filters. The main theme of the present study is two-fold: The first is the improvement of the existing finite difference algorithms developed by Cai (1993) for solving Navier-Stokes equations, and transport equations of the turbulent kinetic energy and viscous dissipation. In particular, the validity of the specification of boundary and initial conditions, numerical stability, and convergence of the solution, will be discussed in detail. The second theme is the effects of the effective thickness and the permeability on the flow field. The significance of this study is that the understanding of the flow field inside the automotive air induction system and the effects of the dust loading may be helpful to develop better

designs of automotive air cleaners. Consequently, the dust holding capacity, filtration efficiency, and endurance of air filters could be improved.

Most of the previous modeling studies simplified the shape of a pleat of an automotive filter as either a triangle (Cai, 1993; Tubbett, 1995) or a square (Chen, et al., 1993). The geometry of an ellipse, which resembles the real form of individual pleats of a filter, makes the finite difference discretization of the computational domain difficult, in particular, for the boundary areas. Instead of considering a single pleat, the present study takes an air filter as a rectangular porous medium with an effective thickness, d , which resembles the height of the filter. This simplification was also used by Gurumoorthy (1990). The upper and lower solid boundaries of the rectangular domain are fixed. A filter or a porous medium is located inside the rectangle. The flow inside the filter is assumed to be laminar and outside the filter is turbulent. For the flow outside the filter, the Reynolds' number, Re , is about 3.78×10^4 , assuming pipe flow with a diameter, D_{in} , 0.1905 m (7.5 inches), maximum inlet velocity, U_{in} , 3.0 m/s, and a kinematic viscosity, ν , 1.508×10^{-5} m²/s ($Re = U_{in} \cdot D_{in} / \nu$). The critical Reynolds number for a pipe flow from laminar to transitional flow regimes is about 2300 (Kays and Crawford, 1993, p. 193-194). Therefore, the flow outside the filter should be fully-developed turbulent flow.

For the air flow inside automotive filters, laminar flow was considered by Gurumoorthy (1990), Cai (1993), and Tebbutt 1995). Gurumoorthy claimed that his results could be checked with experimental results with certain satisfaction. For the air flow considered in the present study, Reynolds number is only about 0.5 for the air

flowing through a filter with velocity of 3 m/s and fiber diameter of 10^{-6} m. According to Rosner (1986), flow is laminar when Re is less than 10 and fully-turbulent when Re is over 3000. Thus, air flow should be laminar inside a automotive filter.

The extended Darcy's law proposed by Vafai and Tien (1981) is applied to the porous medium. The extended Darcy's Law takes into account the inertial forces and viscous dissipation, in addition to the original term of Darcy's law. A standard k- ϵ model is incorporated for the turbulent flow outside the filter. Finite difference methods are adopted to discretize the partial differential equations with the forward difference scheme for the first order derivatives and a combination of the central and upstream schemes for the convection terms in the momentum, turbulent kinetic energy, and viscous dissipation equations.

The present study is conducted based on Cai's work (1993). Cai developed a computer program to model the air flow in a small portion of the filter. Cai's program was designed to solve the two-dimensional momentum, continuity, and transport equations of the turbulent kinetic energy, k, and viscous dissipation, ϵ . Cai's computer program was based on the program SOLA (Hirt et al., 1975) and UV2D [course notes from Lilley (1993)]. Cai treated the flow outside a filter as turbulent flow. The standard k- ϵ model was adopted to predict the mean flow properties like mean velocity, pressure, kinetic energy and dissipation. In addition to Cai's study, Gurumoorthy (1990), Chen et al., (1993) and Tebbutt (1995) have also conducted similar exercises.

The above mentioned studies (except Gurumoorthy, 1990); share the following common ground: 1) Only a half of a pleat is considered which is a very small portion of the filter; 2) The upper and lower boundaries were considered as the free-slip type; 3) The inlet flow is uniform, i.e., $U(y)$ equal to a constant, and the outlet flow has the characteristics of $dU/dx=0$. The main reason to consider only a half of a pleat is that a small computational domain requires less grid points and demands little computer power. However, the results do not describe the whole air induction system.

The major improvement of the present study over the previous work is four-fold. First, the new version of the computer code, TLUV2D, is in a structured modular form, easy to read, understand and make changes to in the future. Cai's program, FILTER, is a non-structured program with many control commands which make the program hard to read. Second, the pressures at boundaries, which were mistakenly taken as zero in Cai's study, are defined by using linear extrapolation. Third, for the calculation of the pressure, all terms are incorporated in the Navier-Stokes equations. Previous studies omitted the terms relevant to the convection and diffusion in the momentum equations. Finally, more reasonable initial conditions for the U- and V-velocities are introduced. The velocity component in the x-direction, U, has a fully-developed profile, and in the y-direction, V, is zero for the whole computational domain. This treatment of the initial condition prevents the continuity law from being violated artificially, and makes the convergence to the steady-state flow regime faster. In Cai's study, the U-velocity initially is a constant at the inlet and is zero for the rest of the computational domain, and the V-velocity is zero. This initial condition may violate the law of continuity.

Through this study, with respect to the development of the algorithms, effects of the permeability, K , time step, Δt , and grid sizes, Δx and Δy , on the velocity distribution and evolution, the following conclusions can be drawn: 1) The CFD algorithm allows the grid size to vary from millimeters to a few meters with the time step less than 100 times smaller than a stability criterion. The time step, Δt , can have a significant effect on the accuracy of the solution. However, it seems that the numerical solution is insensitive to the grid size provided that Δt is in the appropriate range; 2) For an initially fully-developed U-velocity profile, it takes approximately 3 milliseconds (ms) to reach the steady-state and this time period seems independent of Δt and grid size; 3) Pressures almost do not change in the x-direction for the turbulent regime (outside the filter). Linear pressure drops are observed within the filter along the x-axis as predicted from Darcy's law. This result may indicate that the inertial forces on the fluid flow and the viscous diffusion are insignificant for the cases of the present study; 4) The inflow U-velocity profile will be significantly flattened as the flow approaches the filter. Within the filter, the velocity gradients near the wall are very large. This may indicate that viscosity plays a relative unimportant role; 5) The magnitude and distribution of permeability can significantly alter the flow pattern.

1.3 SUMMARY OF CHAPTER 3

Automotive filters are designed to remove the dust from the air passing through the air induction systems of automobiles. Naturally, an understanding of the patterns of the dust distribution inside or on the air filters and the effects of such dust distribution on the velocity distribution of the air flow in an automotive air induction system are of practical

interest to the automotive industry. It is believed that such an understanding will be helpful in the automotive filter design. Consequently, the dust holding capacity will be increased; the filtration efficiency will be improved, and the life span of air filters will be prolonged. In order to achieve such goals, numerous experiments have been conducted. The testing of automotive engine filters is governed by the Society of Automotive Engineers' (SAE) J726 Air Cleaner Test Code (1987). The present study has generally followed the test code.

The main themes of the present study are two-fold: first, through experiments to see how the dust holding capacity responds to increases in the terminating pressure drops. The **terminating pressure drop**, Δp , is defined as the pressure drop in addition to the pressure drop measured for the clean filter with the same volumetric flow rate. The dust holding capacity is referred to as the amount of dust held inside a filter at a given Δp . Note that it is not the ability of a filter to hold dust. During automotive engine operations, with the accumulation of dust onto an air filter, the pressure drop across the air induction system must increase in order to maintain the quantity of air supplied to the engine. The second theme of this study is the effects of the dust loading on velocity distributions. From the theories of fluid flow in porous media (the filter paper or the whole filter may be considered as a porous medium), dust loading on a filter decreases the local permeability of the filter and increases the local resistance to fluid flow, and consequently alters the flow field. It may be expected that non-uniform velocity upstream of the filter and dust distributions should result in preferential dust deposition the filter in regions of higher velocity (Liang et al., 1994). It is anticipated that the dust deposition at the center of a

filter could be higher, by as much as 50%, than that at the edges of the filter. Such an anticipation is based on Liang and co-workers' experimental results tested under the SAE J726 test housing. Liang et al. showed that the particle concentration is higher at low velocity segments than at the high velocity center of the filter. Liang et al. also showed that the particle concentration at the center of the filter is, at the maximum, 4 times lower than that at the edges, while the axial velocity at the center can be as high as 6 times of that at the edges of the filter. Therefore, dust flux at the center of the filter can be higher by as much as 50% than that at the edges. However, it should be remembered that the housing for the LDA velocity measurements is different from that for the dust loading experiments. Therefore, the inlet velocity distribution may be different for the two experiments. The topic of the dust distribution in the automotive air filter is subjected to further study in the future.

The experimental procedure of the present study consists of two parts. The first is dust loading of clean filters to prepare dirty filters for the LDA velocity measurement which is the second part of the experiment. Several studies about dust-loading experiments and LDA velocity measurements of flow field have been conducted (Liang et al., 1994; Newman, 1994; Sabnis et al., 1994a, b; Duran, 1995). The present study is based on the work conducted by Newman (1994) and Sabnis et al. (1994a, b) who carried out a series of LDA velocity measurements for clean panel air filters. The axial velocity distribution from their experiments showed an impinging jet-like profile upstream of the clean filter. The axial velocity decreases dramatically from the center toward the edges. Flow visualization experiments conducted by Newman (1994), Sabnis et al. (1994a), and Duran

(1995) also demonstrated the very non-uniform nature of the velocity field upstream of the filter. Furthermore, separation and re-circulation near the wall were also observed. In the present study, as far as LDA velocity measurements are concerned, only the area directly above the filter is considered. The re-circulation and separation near walls are neglected.

The LDA velocity measurements were conducted at the level 12.7 mm upstream of the filter. Only one half of the filter is measured assuming a symmetrical distribution of the velocity for the other half. The mesh size for the velocity measurement is $12.7 \times 19.05 \text{ mm}^2$. Velocity fields for a clean filter and dirty filters with capacities corresponding to additional pressure drops of 0.127, 0.254, and 0.381 m of water have been measured. The experimental results show that the dust loading does make the velocity profiles less non-uniform; the peaked, impinging jet-like velocity profiles are broadened. Velocity profiles for the design capacity filter remain very non-uniform. The results obtained from this experiment may have implications for the performance of filters installed in vehicle housings. The results may suggest that the velocity distributions presented to filters installed in a vehicle will not change dramatically as the filter accumulates dirt during engine operations. Somewhat more dramatic change of the velocity field as the dust holding exceeds the full designed capacity may indicate that during the latter stage, the preferential deposition of the dust at the center of the filter is magnified. Dust loading at the center of a filter will increase the resistance, and consequently, the magnitude of the velocities at filter center will decrease.

CHAPTER 2

CFD MODELING OF THE AIR FLOW THROUGH POROUS MEDIA USING A K- ϵ MODEL AND THE EXTENDED DARCY'S LAW

ABSTRACT

Most previous studies in predictions of the air flow inside an automotive air induction system considered only a single pleat of an automotive filter. It is obvious that the CFD modeling results from a single pleat of an automotive filter may not describe the whole flow field. In the present study, the automotive filter is considered as a rectangular porous medium with an effective thickness and permeability distribution to describe the characteristics of the filter. The main theme is the prediction of the flow field inside an automotive air induction system using two-dimensional (2D) finite difference schemes, and the effect of the magnitude as well as the distribution of permeability of an automotive filter, in particular, on the redistribution of the inlet flow upstream of the filter. Automotive filter designers desire to have a uniform velocity distribution upstream of the filter. Thus, the dust will uniformly deposit onto the filter during engine operations, and consequently increase the efficiency of the filtration and the dust holding capacity. The permeability is directly related to the magnitude and pattern of the dust loading. The standard k- ϵ model has been applied to the turbulent flow outside the filter. The extended

permeability is directly related to the magnitude and pattern of the dust loading. The standard k- ϵ model has been applied to the turbulent flow outside the filter. The extended Darcy's law, which takes into account both the inertial forces on the fluid and the viscous dissipation, is imposed to account for the laminar flow inside the filter.

From the CFD modeling, the following conclusions can be drawn: 1) The CFD algorithm allows the grid size to vary from millimeters to a few meters with the time step Δt less than 100 times smaller than a stability criterion. The time step, Δt , can have a significant effect on the accuracy of the solution. However, it seems that the numerical solution is insensitive to the grid size, provided that the Δt is in the appropriate range; 2) For an initially fully-developed velocity profile, the flow takes approximately 3 ms to reach the steady-state and this time period seems independent of the Δt and grid size; 3) Pressure drops almost do not change in the x-direction for the turbulent regime (outside the filter). Linear pressure drops are observed within the filter along the x-axis as predicted from Darcy's law. This result may indicate that the inertia forces on the fluid flow and the viscous diffusion are insignificant for the cases of the present study; 4) The fully-developed inlet velocity profile will be significantly flattened as the flow approaches the filter. Within the filter, the velocity gradients near the wall are very large. This may indicate that the viscosity plays a relatively unimportant role. The permeability distribution can alter the flow pattern significantly. Therefore, the present study suggests that to vary the permeability probably is a most efficient measure to control the velocity distribution upstream of an automotive air filter.

2.1 INTRODUCTION

Computational Fluid Dynamics, namely, CFD, is of significant importance in the prediction of the fluid flow in porous media. The application of CFD modeling techniques to porous media covers a very broad range of scientific disciplines, such as, ground water hydrology, petroleum reservoir simulations (Lerch and Thomasen, 1994), geophysics (seismic inversion), packed-bed chemical reactors (Vafai and Tien, 1981), air flow through filters (Cai, 1993), and so on. Most of the situations mentioned above involve complicated geometrical domains, chemical and physical phenomena. These complications make experimental study either very expensive, time consuming, or even impossible to conduct. Consequently, CFD modeling becomes a very important tool to describe complicated flows.

Most commonly, CFD modeling of the fluid flow in a porous medium is achieved by applying the empirical Darcy's law and the laws of the conservation of mass (continuity), momentum and energy. In 1856, H. Darcy, after numerous experiments with a single phase fluid flowing through a porous medium, proposed an empirical relationship between the pressure gradients and velocities in porous media, which reads as the following:

$$\mathbf{V} = -\frac{\mathbf{K}}{\mu} \nabla P \quad (2.1)$$

where \mathbf{V} is a velocity vector and ∇P pressure gradient, K is the permeability of a porous medium and μ the dynamic viscosity of the fluid. Darcy's law has been used for almost one and a half centuries. Its simplicity and feasibility for a wide range of applications have been generally recognized. However, Darcy's law neglected the effects of solid boundary or inertial forces on fluid flow and heat transfer through porous media or viscous diffusion (Scheidegger, 1974; Carman, 1956; Collins, 1961). These effects can be significant near the walls of pores and in high porosity media. Brinkman (1947) proposed the approximation of the viscous dissipation or heat transfer on the boundaries by the addition of a viscous term to Darcy's law. Muskat (1946) included the velocity squared term to account for the inertial forces. However, neither in Brinkman's nor in Muskat's work had the factors of the inertial forces and viscous dissipation been accounted for simultaneously. Vafai and Tien (1981) proposed an extended Darcy's law taking into account both the inertial forces and the viscous dissipation. The extended Darcy's law reads:

$$\nabla \langle P \rangle = \frac{\mu}{K} \langle \mathbf{V} \rangle + \mu \nabla^2 \langle \mathbf{V} \rangle + b (\langle \mathbf{V} \rangle \cdot \langle \mathbf{V} \rangle) \cdot \mathbf{J} \quad (2.2)$$

where \mathbf{J} is a unit vector and is defined as: $\mathbf{J} = \langle \mathbf{V} \rangle / |\langle \mathbf{V} \rangle|$. b is a constant that depends on the property of a porous medium. The second and the third terms in Eq. (2.2) are viscous and inertial terms, respectively. The symbol $\langle \cdot \rangle$ denotes a volume average property of the porous medium which is defined as Eq (2.3):

$$\langle \Psi \rangle = \frac{1}{V_o} \int \Psi dV_o \quad (2.3)$$

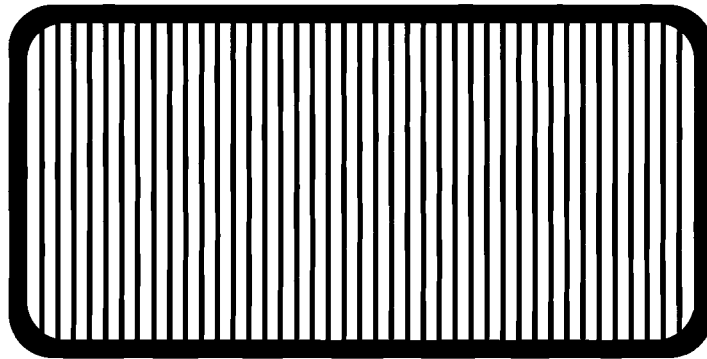
where V_0 is the considered volume over which the property Ψ is averaged.

The present study intends to predict the flow field around an automotive air filter as shown in Figure 2.1, assuming that the flow is two-dimensional. The upper and lower boundaries presented in Figure 2.1 are assumed to be connected to the solid walls of the automotive air induction system. The filter is made of pleated filter media (a kind of fibrous paper) supported by a wire net encased in a rubberized frame. A filter generally contains two parts, pleats and their supporting base. The shapes of individual pleats, by and large, look like elliptical as illustrated in Figure 2.2A.

The main objective of the present study is, by using the technique of CFD modeling, to understand the flow field near the filter in an automotive air induction system. The main theme of the present study is two-fold: The first is the improvement of the existing algorithms developed by Cai (1993) for solving Navier-Stokes equations, transport equations of the turbulent kinetic energy and viscous dissipation, using finite difference schemes. In particular, the validity of the specification of the boundary and initial conditions, the numerical stability, and the convergence of the solution, will be discussed in detail. The second theme is the effects of the effective thickness and the permeability of the filter on the flow field. We know that the dust will deposit on the automotive filter during engine operations. The dust-loading decreases the permeability of the filter, and consequently, increases the resistance of the filter to fluid flow. Thus, the flow distribution changes. It is of practical interest to investigate the permeability effects

on fluid flow, because permeability is related to the amount of dust deposited onto the filter.

Top View



Side View



Figure 2.1 The top and side views of the Purolator AF3192 filter. The pleats are 3 cm high with a 3 mm pitch. The media is about $635\mu\text{m}$ thick.

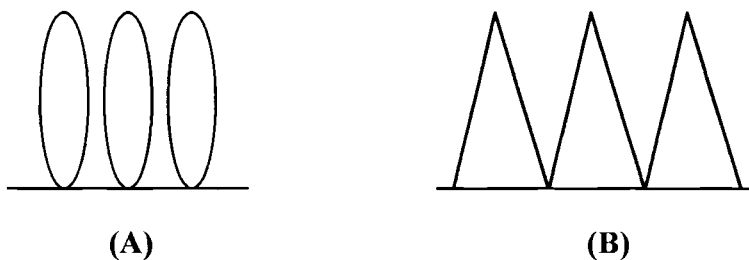


Figure 2.2 The shape of single pleat in an air filter. (A) is the approximate real form of pleats with each pleat in an elliptical shape. (B) is the pleats used by Cai (1993) with each pleat in a triangular shape.

Most of the previous modeling studies simplified the shape of a pleat as either a triangle (Cai, 1993; Tebbutt, 1995) or a rectangle (Chen, et al., 1993). The geometry of an ellipse which resembles the real form of the individual pleat of a filter, makes the finite difference discretization difficult, in particular, for the boundary areas. The CFD modeling result from a single pleat may not describe the flow field around an air filter, because a single pleat occupies only a small portion of the filter. Instead of considering a single pleat, the present study takes an air filter as a rectangular porous medium with an effective thickness d which resembles the height of the filter. This simplification was also used by Gurumoorthy (1990). The computational domain is illustrated in Figure 2.3. The domain is rectangular, with upper and lower solid boundaries fixed. A filter or porous medium is located inside the rectangle. If Figure 2.3 is turned 90 degrees, it will resemble the side view of Figure 2.1. Each side of the filter is connected to the solid walls of an automotive air induction system.

The flow inside the filter is assumed to be laminar and outside the filter is turbulent. For the flow outside the filter, the Reynolds' number R_e is about 3.78×10^4 , assuming a pipe flow with a diameter D_{in} of 0.1905 m (7.5 inches), maximum inlet velocity U_{in} 3.0 m/s, and a kinematic viscosity ν of 1.508×10^{-5} m²/s ($R_e = U_{in} \cdot D_{in} / \nu$). The critical Reynolds number for a pipe flow from laminar to transitional flow regimes is about 2300 (Kays and Crawford, 1993). Therefore, the flow outside the filter should be fully-developed turbulent flow.

For the flow inside the filter, laminar flow was considered by Gurumoorthy (1990),

Cai (1993), and Tebbutt 1995). Gurumoorthy claimed that his results could be checked with experimental results with certain satisfaction. However, it should be remembered that the original Darcy's work concerned only liquid fluids. The gas flow inside porous media can be turbulent as occurs in gas reservoir (Slider, 1976). However, Slider did not propose any turbulent model. Instead, an extended Darcy's law was utilized to calculate the pressure drops in the gas reservoir. Nevertheless, for the flow considered in this study, Reynolds number is only about 0.5 for the air flowing through a filter with velocity of 3 m/s and fiber diameter of 10^{-6} m. According to Rosner (1986), flow is laminar when Re is less than 10 and fully-turbulent when Re is over 3000. Thus, air flow should be laminar inside a automotive filter.

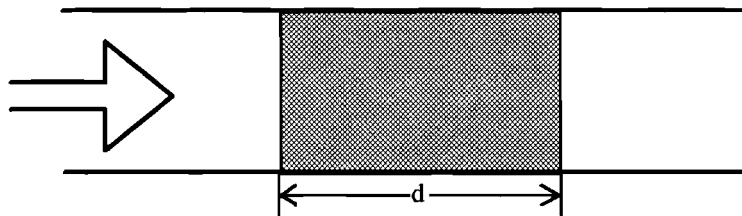


Figure 2.3 A sketch of the computational domain. The shaded area is a porous medium. d , is the effective filter thickness.

The present study is conducted based on Cai's work (1993). Cai developed a computer program, named FILTER, to model the air flow in a small portion of the filter. Cai's FILTER was designed to solve the two-dimensional, momentum, continuity, and transport equations of the turbulent kinetic energy, k , and viscous dissipation, ϵ , using finite difference methods. The computer program was based on the program SOLA (Hirt et al., 1975) and UV2D [CFD course notes from Lilley (1993)]. Cai treated the flow outside a filter as turbulent flow. The standard k - ϵ model [detailed equations can be found

in most texts, for example, Wilcox (1993)] was adopted by Cai to predict the mean flow properties, such as mean velocity, pressure, turbulent kinetic energy and viscous dissipation.

In addition to Cai's study (1993), Gurumoorthy (1990), Chen et al. (1993), and Tebbutt (1995) have also conducted similar exercises. Gurumoorthy intended to predict the air flow in an automobile air induction system using a commercial CFD code, PHOENICS. The program PHOENICS was developed by CHAM Ltd. of London, United Kingdom. The program is capable of modeling multi-dimensional flow phenomena at steady-state. Gurumoorthy applied PHOENICS to calculate three-dimensional air flow inside an automotive air induction system. He also used the standard k- ϵ model for the turbulent flow regime. Gurumoorthy claimed that his computational results could be checked by the experimental results with certain satisfaction.

Chen et al. (1993) investigated the air flow through pleated filters using a finite element method in two-dimensional space coordinates. Chen and co-coworkers considered one half of a single filter pleat which was approximated by a rectangle. The inertial forces on the fluid in the filter were neglected, because of the low velocity flow field. Consequently, they predicted that a linear relationship existed between the pressure drop and velocity, as stated in Darcy's law. Tebbutt (1995) used the same extended Darcy's law as Cai (1993) to model the fluid flow inside a pleat, and Prandtl's mixing length model to describe the turbulent flow outside the pleat. Tebbutt also conducted

experiments to determine the parameters K and inertial factor, b in the extended Darcy's law with flat filter paper mounted inside a pipe.

The above mentioned studies (except Gurumoorthy, 1990) all share the following common ground: 1) only a half of a pleat is considered which is a very small portion of the filter; 2) the upper and lower boundaries were considered as free-slip type; 3) the inlet flow is uniform i.e. $U(y)$ equal to a constant, and outlet flow has the characteristics of dU/dx equal to zero. The main reason to consider only one half of a pleat is that the small computational domain requires fewer grid points and demands little computer power. However, the results may not describe the whole air induction system.

Being aware of the advantages and drawbacks of the previous works, in the present study, I intended to model the flow field for the automotive air induction system with a rectangle. Non-slip conditions are introduced for the upper and lower boundaries. Obviously, a compromise is made between reality and simplicity. Furthermore, instead of concentrating on a single pleat, I avoided consideration of the microstructure of the filter and considered a filter as a continuous porous medium with an equivalent or effective thickness which is less than the height of the filter. It is assumed that the rectangular porous medium can play the same role as a filter.

The improvement of the present study over the previous works is four-fold. First, the new version of the FORTRAN code named TLUV2D is in a structured modular form, easy to read, understand and make changes to in the future. The program FILTER is a non-structured program with many control commands which make the program hard to

read. Second, the pressures at boundaries are defined using linear extrapolation. They were mistakenly undefined in Cai's study. Therefore, during the program execution, computer will taken these pressures on the upper and right hand side boundaries as zero. It should be noted that the derivatives of the pressure with respect to x and y are first order, and the forward difference method needs only the pressure values in the upper and right boundary cells to be defined. Third, for the calculation of the pressure, all terms are incorporated in the Navier-Stokes equations. Previous studies omitted the terms relevant to the convection and diffusion. This subject is considered in the discussion. Finally, more reasonable initial conditions for the U- and V-velocity are introduced. The U-velocities have fully-developed profiles in the x-direction and the velocity component in the y-direction, V, equals zero for the whole computational domain. This treatment of the initial condition prevents the continuity law from being violated artificially, and makes the convergence to the steady-state flow regime faster.

2.2 PARTIAL DIFFERENTIAL EQUATIONS

The present study concerns relatively low velocity air flow (about 3 m/s) and approximately constant temperature in order to maintain the nature of a constant property flow. The flow regime is two-dimensional and obeys the laws of conservation of mass (continuity), momentum and energy. Because of the constant properties of density and viscosity, the energy equations can be decoupled from the momentum and continuity equations. The energy equation is not solved in this study. As stated in the previous section, the flow regime inside the filter is considered laminar flow and governed by the extended Darcy's law (Vafai and Tien, 1981). The turbulent flow outside the filter region is assumed to be modeled by a standard k-ε model.

2.2.1 Equations for Laminar Flow

Vafai and Tien (1981) proposed the use of volume averaged properties for the fluid flow in a porous medium, because of the chaotic nature of the fluid flow in a porous medium. Using the volume average velocities, the continuity and momentum equations can be expressed as Eqs. (2.4) and (2-5), respectively:

$$\text{Continuity Equation:} \quad \nabla \cdot \langle \mathbf{V} \rangle = 0 \quad (2.4)$$

Momentum Equation:

$$\rho \frac{D\langle \mathbf{V} \rangle}{Dt} = -\nabla \langle P \rangle^f + \mathbf{g} + \mu \nabla^2 \langle \mathbf{V} \rangle - \frac{\mu}{K} \langle \mathbf{V} \rangle + \mathbf{b}(\langle \mathbf{V} \rangle \cdot \langle \mathbf{V} \rangle) \cdot \mathbf{J} \quad (2.5)$$

where the material derivative on the left hand of Eq. (2.5) takes the form:

$$\frac{D}{Dt} = U \frac{\partial}{\partial x} + V \frac{\partial}{\partial y} \quad (2.6)$$

The pressure gradient on the right hand of Eq. (2.5) is the fluid pressure gradient. The last term of Eq. (2.5) accounts for the inertial forces on the fluid. The scalar forms for the continuity and momentum equations in 2D Cartesian coordinates can be defined as Eqs. (2-7)-(2-8), respectively:

$$\text{Continuity:} \quad \frac{\partial U}{\partial x} + \frac{\partial V}{\partial y} = 0 \quad (2.7)$$

Momentum Equations in x and y directions:

$$\text{x-direction:} \quad \frac{DU}{Dt} = -\frac{\phi}{\rho} \frac{\partial P}{\partial x} + g_x + v \nabla^2 U - \frac{v\phi}{K} U - \frac{b}{2} U \sqrt{U^2 + V^2} \quad (2.8)$$

$$\text{y-direction:} \quad \frac{DV}{Dt} = -\frac{\phi}{\rho} \frac{\partial P}{\partial y} + g_y + v \nabla^2 V - \frac{v\phi}{K} V - \frac{b}{2} V \sqrt{U^2 + V^2} \quad (2.9)$$

where U and V are velocity components in the x- and y-direction, and g_x and g_y are gravitational acceleration in the x- and y-direction, respectively. ϕ is the porosity of the porous media. The last two terms in Eqs. (2-8) and (2-9) are contributions from Darcy's law and the inertia of the fluid. It should be mentioned that the last term can be important only for relatively high velocity flow and high porosity media. The term of the viscous dissipation has the same form as the term of diffusion in the momentum equations. The two terms are combined together to form the third term in Eqs. (2.8) and (2.9).

2.2.2 Equations for Turbulent Flow

It is well-known that turbulent properties can be decomposed into the mean property which is derived from the time average of a turbulent property and the fluctuating part. The most popular way to decompose a turbulent property is the Reynolds' decomposition in the form of Eq. (2.10):

$$W = \overline{W} + w \quad (2.10)$$

where W , \overline{W} , w are the instantaneous, mean, and fluctuating part of a turbulent property, respectively. Substituting Eq. (2-10) into the instantaneous continuity and momentum equations for laminar flow and taking averages yields continuity and momentum equations for turbulent flow:

Continuity:
$$\frac{\partial \overline{U}}{\partial x} + \frac{\partial \overline{V}}{\partial y} = 0 \quad (2.11)$$

Momentum Equations:

x-direction:
$$\frac{D\overline{U}}{Dt} = -\frac{1}{\rho} \frac{\partial P}{\partial x} + g_x + \nu \nabla^2 \overline{U} + \tau_x \quad (2.12)$$

where τ_x , is a turbulent stress derived from the convection terms and is in the form of:

$$\tau_x = -\left(\frac{\partial \overline{uu}}{\partial x} + \frac{\partial \overline{uv}}{\partial y} \right) \quad (2.13)$$

It is well-known that $-\overline{\rho u_i u_j}$ is the Reynolds-stress tensor. After Boussinesq's concept of using the mean velocity gradient to approximate the turbulent stresses as the case in the

laminar flow, Hinze (1975) showed that:

$$-\overline{u_i u_j} = -\frac{2}{3} k \delta_{ij} + \mu_t \left(\frac{\partial \bar{U}_i}{\partial x_j} + \frac{\partial \bar{U}_j}{\partial x_i} \right) \quad (2.14)$$

where k is the turbulent kinetic energy and δ is the Kronecker delta. μ_t is the turbulent or eddy viscosity with the same dimension as the dynamic viscosity of the laminar flow. For two-dimensional flow i and j vary from 1 to 2, with 1 denoting the x-direction and 2 the y-direction. The second term on the right hand of Eq (2.14) is the mean strain rate tensor which will vanish as i equals j for incompressible flow. Thus, the first term is needed to obtain the proper trace of the Reynolds stress tensor. Eq. (2-14) is applicable to Newtonian flow. For non-Newtonian fluid flow the relationship of Eq. (2.14), by and large, are not appropriate. One must remember that the introduction of eddy viscosity concept does not yield a complete solution to the turbulent flow, as pointed out by Hinze (1975). For instance, the results predicted by Eq.(2.14) are not agree with experimental results for a one-dimensional flow. More details about the approximation of Reynolds stress can be referred from Hinze (1975) and Wilcox (1993).

Substituting Eq. (2.14) into (2.13), we have:

$$\tau_x = \frac{\partial}{\partial x} \left[v_t \left(\frac{\partial \bar{U}}{\partial x} + \frac{\partial \bar{U}}{\partial x} \right) - \frac{2}{3} k \right] + \frac{\partial}{\partial x} \left[v_t \left(\frac{\partial \bar{U}}{\partial y} + \frac{\partial \bar{V}}{\partial x} \right) \right] \quad (2.15)$$

where $v_t = \mu_t / \rho$ is the turbulent kinematic viscosity. The momentum equation in the y-

direction can be expressed as Eq. (2-16):

$$\text{y-direction: } \frac{D\bar{V}}{Dt} = -\frac{1}{\rho} \frac{\partial P}{\partial y} + g_y + \nu \nabla^2 \bar{V} + \tau_y \quad (2.16)$$

where τ_y is the turbulent stress and can be expressed as:

$$\begin{aligned} \tau_y &= -\left(\frac{\partial \overline{uv}}{\partial x} + \frac{\partial \overline{vv}}{\partial y} \right) \\ &= \frac{\partial}{\partial x} \left[\nu_t \left(\frac{\partial \bar{U}}{\partial y} + \frac{\partial \bar{V}}{\partial x} \right) \right] + \frac{\partial}{\partial y} \left[\nu_t \left(\frac{\partial \bar{V}}{\partial y} + \frac{\partial \bar{V}}{\partial y} \right) - \frac{2}{3} k \right] \end{aligned} \quad (2.17)$$

The turbulent kinetic energy equation can be expressed as Eq. (2.18). The detailed derivations and explanations can be found in the text of Wilcox (1993) and Hinze (1975):

$$\frac{Dk}{Dt} = \frac{\partial}{\partial x_j} \left[\left(\nu + \frac{\nu_t}{\sigma_k} \right) \frac{\partial k}{\partial x_j} \right] + \nu_t \frac{\partial \bar{U}_i}{\partial x_j} \left(\frac{\partial \bar{U}_i}{\partial x_j} + \frac{\partial \bar{U}_j}{\partial x_i} \right) - \varepsilon \quad (2.18)$$

where the subscripts i and j vary from 1 to 2 with 1 and 2 denoting x - and y -direction, respectively.

The turbulent dissipation equation:

$$\begin{aligned} \frac{D\varepsilon}{Dt} &= \frac{\partial}{\partial x_j} \left[\left(\nu + \frac{\nu_t}{\sigma_\varepsilon} \right) \frac{\partial \varepsilon}{\partial x_j} \right] + \\ &C_{1\varepsilon} \frac{\varepsilon}{k} \nu_t \frac{\partial \bar{U}_i}{\partial x_j} \left(\frac{\partial \bar{U}_i}{\partial x_j} + \frac{\partial \bar{U}_j}{\partial x_i} \right) - C_{2\varepsilon} \frac{\varepsilon^2}{k} \end{aligned} \quad (2.19)$$

$$v_t = C_\mu \frac{k^2}{\varepsilon} \quad (2.20)$$

where i and j have the same meanings as in Eq. (2.18). σ_k , σ_ε , $C_{1\varepsilon}$, $C_{2\varepsilon}$, and C_μ , are empirical constants. The values used in the present study are listed in Table 2.1. Rodi (1980) suggested that these empirical constants for the standard k - ε model applied best to the high Reynolds number turbulent flow. These empirical constants may vary with flow regimes. For instance, σ_ε equal 1.22 was used by Comini and Giudice (1985).

It should be noted that the eddy viscosity concept is applied again in Eqs. (2.18) and (2.19). Equation. (2.20) is derived based on the mixing length theory and the transport equation of the turbulent kinetic energy. The detailed derivations and explanations are provided in the text of Kays and Crawford (1993, p. 217-221).

C_μ	$C_{1\varepsilon}$	$C_{2\varepsilon}$	σ_k	σ_ε
0.09	1.44	1.92	1.0	1.3

Table 2.1 The constants used in the standard k - ε model (after Rodi, 1980)

It should be noted that the k - ε model provides an approximation for the turbulent viscosity. Substituting the value of the turbulent viscosity into the turbulent momentum equations, the mean flow velocities, and pressures can be obtained as in laminar flow. In such a way, the turbulent equations (continuity and momentum) are closed, i.e. the number of unknowns equals the number of equations.

2.3 FINITE DIFFERENCE EQUATIONS

Following Hirt et al., (1975), the computational domain is discretized into a mesh as illustrated in Figure 2.4. The boundary cells (shaded area) are fictitious. The arrangement of variables is depicted in Figure 2.5. From the figure, it can be seen that pressure, the turbulent kinetic energy, k , turbulent dissipation, ϵ , and turbulent viscosity are located in the geometrical center of a mesh. Velocities are assigned at the middle point of each side boundary of a mesh. This is called the Marker-and-Mesh method to arrange the variables. This method was first introduced by Harlow and Welch (1965).

2.3.1 Laminar Flow

For the discretization of the continuity equation and the pressure terms in the momentum equations, the forward difference scheme is utilized. The convection terms in the momentum equations are discretized using the combination of the central difference and the ‘upwind’ or upstream schemes. The weight of the upstream schemes is controlled by the factor α (in Eqs. [2.24)-(2.27]). When α equals zero, the convection terms will be discretized by the central scheme. It is well-known that the central scheme can have the instability problem, if the selection of the time step is inappropriate, but the pure upstream scheme introduces some unnecessary calculations (Hirt et al., 1975). The momentum equations are discretized using the explicit method with respect to time derivatives. Discretization of Eq. (2.7), the continuity equation, using a forward difference scheme yields:

Continuity:
$$\frac{U_{i,j}^{n+1} - U_{i-1,j}^{n+1}}{\Delta x} + \frac{V_{i,j}^{n+1} - V_{i,j-1}^{n+1}}{\Delta y} = 0 \quad (2.21)$$

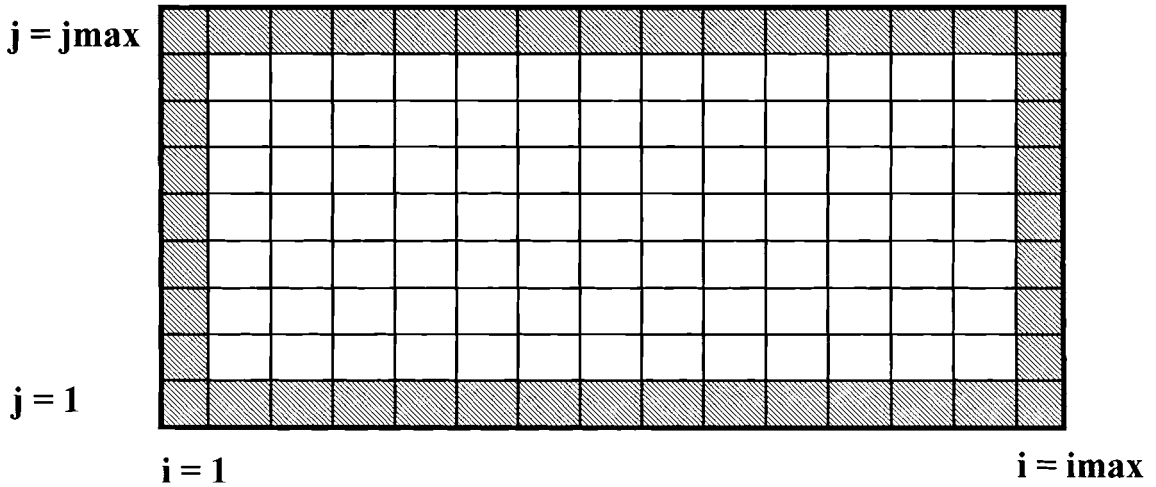


Figure 2.4 A sketch of the discretization of the computational domain into cells.

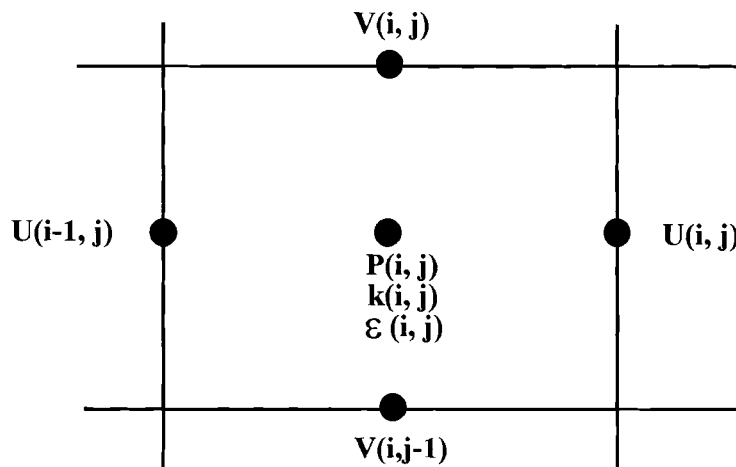


Figure 2.5 A sketch showing the nodes and nodal variable locations for the cell (i, j) (after Hirt et al. 1975).

where superscript $n+1$ denotes $n+1$ time increments after the initiation. Δx and Δy are the grid spaces in the x - and y -directions for cell (i,j) , respectively. The finite difference form of the momentum equations (2.8) and (2.9) are in the forms of (2.22) and (2.23), respectively:

$$U_{i,j}^{n+1} = U_{i,j}^n + \Delta t \left\{ \frac{\phi}{\Delta x} (P_{i,j}^n - P_{i+1,j}^n) + g_x - \Omega_x^u - \Omega_y^u + \Gamma_u + D_x + I_x \right\} \quad (2.22)$$

$$V_{i,j}^{n+1} = V_{i,j}^n + \Delta t \left\{ \frac{\phi}{\Delta y} (P_{i,j}^n - P_{i,j+1}^n) + g_y - \Omega_x^v + \Omega_y^v - \Gamma_v + D_y + I_y \right\} \quad (2.23)$$

where ϕ is the porosity of the cell (i,j) , and:

$$\begin{aligned} \Omega_x^u &= \frac{\partial U^2}{\partial x} \\ &= \frac{1}{4\Delta x} \left\{ (U_{i,j} + U_{i+1,j})^2 + \alpha |U_{i,j} + U_{i+1,j}| (U_{i,j} - U_{i+1,j}) \right. \\ &\quad \left. - (U_{i-1,j} + U_{i,j})^2 - \alpha |U_{i-1,j} + U_{i,j}| (U_{i-1,j} - U_{i,j}) \right\} \end{aligned} \quad (2.24)$$

$$\begin{aligned} \Omega_y^u &= \frac{\partial(UV)}{\partial y} \\ &= \frac{1}{4\Delta y} \left\{ (U_{i,j} + U_{i,j+1})(V_{i,j} + V_{i+1,j}) + \alpha (U_{i,j} - U_{i,j+1}) |V_{i,j} + V_{i+1,j}| \right. \\ &\quad \left. - (U_{i,j} + U_{i,j-1})(V_{i,j-1} + V_{i+1,j-1}) - \alpha (U_{i,j-1} - U_{i,j}) |V_{i,j-1} + V_{i+1,j-1}| \right\} \end{aligned}$$

(2.25)

$$\begin{aligned}
\Omega_x^y &= \frac{\partial(UV)}{\partial x} \\
&= \frac{1}{4\Delta x} \left[(U_{i,j} + U_{i,j+1})(V_{i,j} + V_{i,j+1}) + \alpha |U_{i,j} + U_{i,j+1}| (V_{i,j} + V_{i,j+1}) \right. \\
&\quad \left. - (U_{i-1,j} + U_{i-1,j+1})(V_{i-1,j} + V_{i,j}) - \alpha |U_{i,j} + U_{i,j+1}| (V_{i-1,j} - V_{i,j}) \right]
\end{aligned}
\tag{2.26}$$

$$\begin{aligned}
\Omega_y^y &= \frac{\partial V^2}{\partial y} \\
&= \frac{1}{4\Delta y} \left[(V_{i,j} + V_{i,j+1})^2 + \alpha |V_{i,j} + V_{i,j+1}| (V_{i,j} - V_{i,j+1}) \right. \\
&\quad \left. - (V_{i,j-1} + V_{i,j})^2 - \alpha |V_{i,j-1} + V_{i,j}| (V_{i,j-1} - V_{i,j}) \right]
\end{aligned}
\tag{2.27}$$

$$\begin{aligned}
\Gamma_x &= v \left(\frac{\partial^2 U}{\partial x^2} + \frac{\partial^2 U}{\partial y^2} \right) \\
&= v \left(\frac{1}{\Delta x^2} (U_{i+1,j} - 2U_{i,j} + U_{i-1,j}) + \frac{1}{\Delta y^2} (U_{i,j+1} - 2U_{i,j} + U_{i,j-1}) \right)
\end{aligned}
\tag{2.28}$$

$$\begin{aligned}
\Gamma_y &= v \left(\frac{\partial^2 V}{\partial x^2} + \frac{\partial^2 V}{\partial y^2} \right) \\
&= v \left(\frac{1}{\Delta x^2} (V_{i+1,j} - 2V_{i,j} + V_{i-1,j}) + \frac{1}{\Delta y^2} (V_{i,j+1} - 2V_{i,j} + V_{i,j-1}) \right)
\end{aligned}
\tag{2.29}$$

$$D_x = -\frac{v}{K} U_{i,j} \quad (2.30)$$

$$D_y = -\frac{v}{K} V_{i,j} \quad (2.31)$$

$$I_x = -\frac{1}{2} b \cdot U_{i,j} \cdot \sqrt{U_{i,j}^2 + V_{i,j}^2} \quad (2.32)$$

$$I_y = -\frac{1}{2} b \cdot V_{i,j} \cdot \sqrt{U_{i,j}^2 + V_{i,j}^2} \quad (2.33)$$

The terms on the right hands of Eqs. (2.24)-(2.33) are from the last time step or they should have the superscript n. The expression for pressure is obtained by substituting Eqs. (2-22) and (2-23) into (2.21) and can be expressed as:

$$P_{i,j} = \left[\frac{P_{i+1,j}}{\Delta x^2} + \frac{P_{i,j+1}}{\Delta y^2} \right] / \beta - \left(C - \frac{\Theta_u}{\Delta x} - \frac{\Theta_v}{\Delta y} \right) / (\Delta t \phi \beta) \quad (2.34)$$

where:

$$C = \frac{U_{i,j}^n - U_{i-1,j}^{n+1}}{\Delta x} + \frac{V_{i,j}^n - V_{i,j-1}^{n+1}}{\Delta y} \quad (2.35)$$

$$\beta = 1/\Delta x^2 + 1/\Delta y^2$$

$$\Theta_u = g_x - \Omega_x^u - \Omega_y^u + \Gamma_u + D_x - I_x \quad (2.36)$$

$$\Theta_v = g_y - \Omega_y^v - \Omega_y^v + \Gamma_v + D_y - I_y \quad (2.37)$$

2.3.2 Turbulent Flow

Discretization of the continuity and momentum equations for the turbulent flow shares the same principles as for the laminar flow. The forward difference scheme is applied to the continuity and pressure derivatives, and a combination of the central difference and the upstream difference is used for convection terms.

$$\text{Continuity: } \frac{\bar{U}_{i,j}^{n+1} - \bar{U}_{i-1,j}^{n+1}}{\Delta x} + \frac{\bar{V}_{i,j}^{n+1} - \bar{V}_{i,j-1}^{n+1}}{\Delta y} = 0. \quad (2.38)$$

Discretization of Eqs. (2.12) and (2.16) of the momentum equations yield Eqs. (2.39) and (2.40) for the x- and y-directions, respectively:

$$\bar{U}_{i,j}^{n+1} = \bar{U}_{i,j}^n + \Delta t \left[\frac{1}{\Delta x} (P_{i,j}^n - P_{i+1,j}^n) + g_x - \Omega_x^{\bar{u}} - \Omega_y^{\bar{u}} + \Gamma_{\bar{u}} + \tau_x \right] \quad (2.39)$$

$$\bar{V}_{i,j}^{n+1} = \bar{V}_{i,j}^n + \Delta t \left[\frac{1}{\Delta y} (P_{i,j}^n - P_{i,j+1}^n) + g_y - \Omega_x^{\bar{v}} - \Omega_y^{\bar{v}} + \Gamma_{\bar{v}} + \tau_y \right] \quad (2.40)$$

where:

$\Omega_x^{\bar{u}}, \Omega_y^{\bar{u}}, \Omega_x^{\bar{v}}, \Omega_y^{\bar{v}}, \Gamma_{\bar{u}}, \Gamma_{\bar{v}}$ have the form as $\Omega_x^u, \Omega_y^u, \Omega_x^v, \Omega_y^v, \Gamma_u, \Gamma_v$ of the laminar flow, except that the velocity components U and V are replaced by \bar{U} and \bar{V} . τ_x and τ_y are Reynolds stresses and can be expressed as Eqs. (2.41) and (2.42), respectively:

$$\begin{aligned}
\tau_x &= -\left(\frac{\partial \overline{uu}}{\partial x} + \frac{\partial \overline{uv}}{\partial y}\right) \\
&= \frac{\partial}{\partial x} \left[v_t \left(\frac{\partial \overline{U}}{\partial x} + \frac{\partial \overline{U}}{\partial x} \right) - \frac{2}{3} k \delta_{11} \right] + \frac{\partial}{\partial y} \left[v_t \left(\frac{\partial \overline{V}}{\partial x} + \frac{\partial \overline{U}}{\partial y} \right) - \frac{2}{3} k \delta_{12} \right]
\end{aligned} \tag{2.41}$$

$$\begin{aligned}
\tau_y &= -\left(\frac{\partial \overline{uv}}{\partial x} + \frac{\partial \overline{vv}}{\partial y}\right) \\
&= \frac{\partial}{\partial x} \left[v_t \left(\frac{\partial \overline{V}}{\partial x} + \frac{\partial \overline{U}}{\partial y} \right) - \frac{2}{3} k \delta_{12} \right] + \frac{\partial}{\partial y} \left[v_t \left(\frac{\partial \overline{V}}{\partial y} + \frac{\partial \overline{V}}{\partial y} \right) - \frac{2}{3} k \delta_{22} \right]
\end{aligned} \tag{2.42}$$

Discretization of Eq (2.18), the kinetic equation, yields:

$$\mathbf{k}_{i,j}^{n+1} = \mathbf{k}_{i,j}^n + \Delta t \left\{ -\Omega_u^k - \Omega_v^k + \Gamma_k + \Lambda_k - \varepsilon \right\} \tag{2.43}$$

where:

$$\begin{aligned}
\Omega_u^k &= \frac{\partial(\overline{U}k)}{\partial x} \\
&= \frac{1}{2\Delta x} \left\{ \overline{U}_{i,j} (k_{i,j} + k_{i+1,j}) + \alpha |\overline{U}_{i,j}| (k_{i,j} - k_{i+1,j}) \right. \\
&\quad \left. - \overline{U}_{i-1,j} (k_{i-1,j} + k_{i,j}) - \alpha |\overline{U}_{i-1,j}| (k_{i-1,j} - k_{i,j}) \right\}
\end{aligned} \tag{2.44}$$

$$\begin{aligned}
\Omega_v^k &= \frac{\partial(\overline{V}k)}{\partial y} \\
&= \frac{1}{2\Delta y} \left\{ \overline{V}_{i,j} (k_{i,j} + k_{i,j+1}) + \alpha |\overline{V}_{i,j}| (k_{i,j} - k_{i,j+1}) \right. \\
&\quad \left. - \overline{V}_{i,j-1} (k_{i,j} + k_{i,j-1}) - \alpha |\overline{V}_{i,j-1}| (k_{i,j-1} - k_{i,j}) \right\}
\end{aligned} \tag{2.45}$$

$$\begin{aligned}
\Gamma_k &= \frac{\partial}{\partial x_i} \left\{ \left(v + \frac{v_t}{\sigma_k} \right) \frac{\partial k}{\partial x_i} \right\} \\
&= \left(v + \frac{v_t}{\sigma_k} \right) \left(\frac{\partial^2 k}{\partial x^2} + \frac{\partial^2 k}{\partial y^2} \right) + \frac{1}{\sigma_k} \left(\frac{\partial k}{\partial x} \frac{\partial v_t}{\partial x} + \frac{\partial k}{\partial y} \frac{\partial v_t}{\partial y} \right)
\end{aligned} \tag{2.46}$$

$$\begin{aligned}
\Lambda_k &= v_t \frac{\partial \bar{U}_i}{\partial x_j} \left(\frac{\partial \bar{U}_i}{\partial x_j} + \frac{\partial \bar{U}_j}{\partial x_i} \right) \\
&= v_t \left\{ \left(\frac{\partial \bar{U}}{\partial x} \right)^2 + \left(\frac{\partial \bar{V}}{\partial y} \right)^2 + \left(\frac{\partial \bar{U}}{\partial y} \right)^2 + \left(\frac{\partial \bar{V}}{\partial x} \right)^2 + 2 \frac{\partial \bar{U}}{\partial y} \frac{\partial \bar{V}}{\partial x} \right\}
\end{aligned} \tag{2.47}$$

Discretization of Eq. (2.19), the transport equation of the viscous dissipation yields:

$$\varepsilon_{i,j}^{n+1} = \varepsilon_{i,j}^n + \Delta t \left\{ -\Omega_u^\varepsilon - \Omega_v^\varepsilon + \Gamma_\varepsilon + \Lambda_\varepsilon \right\} \tag{2.48}$$

$$\begin{aligned}
\Omega_u^\varepsilon &= \frac{\partial(\bar{U}\varepsilon)}{\partial x} \\
&= \frac{1}{2\Delta x} \left\{ \bar{U}_{i,j} (\varepsilon_{i,j} + \varepsilon_{i+1,j}) + \alpha |\bar{U}_{i,j}| (\varepsilon_{i,j} - \varepsilon_{i+1,j}) \right. \\
&\quad \left. - \bar{U}_{i-1,j} (\varepsilon_{i-1,j} + \varepsilon_{i,j}) + \alpha |\bar{U}_{i-1,j}| (\varepsilon_{i-1,j} - \varepsilon_{i,j}) \right\}
\end{aligned} \tag{2.49}$$

$$\begin{aligned}
\Omega_v^\varepsilon &= \frac{\partial(\bar{V}\varepsilon)}{\partial y} \\
&= \frac{1}{2\Delta y} \left\{ \bar{V}_{i,j} (\varepsilon_{i,j} + \varepsilon_{i,j+1}) + \alpha |\bar{V}_{i,j}| (\varepsilon_{i,j} - \varepsilon_{i,j+1}) \right. \\
&\quad \left. - \bar{V}_{i,j-1} (\varepsilon_{i,j} + \varepsilon_{i,j-1}) - \alpha |\bar{V}_{i-1,j}| (\varepsilon_{i,j-1} - \varepsilon_{i,j}) \right\}
\end{aligned} \tag{2.50}$$

$$\Gamma_{\varepsilon} = \frac{\partial}{\partial x_i} \left\{ \left(v + \frac{v_t}{\sigma_{\varepsilon}} \right) \frac{\partial \varepsilon}{\partial x_i} \right\} \quad (2.51)$$

$$= \left(v + \frac{v_t}{\sigma_{\varepsilon}} \right) \left(\frac{\partial^2 \varepsilon}{\partial x^2} + \frac{\partial^2 \varepsilon}{\partial y^2} \right) + \frac{1}{\sigma_{\varepsilon}} \left(\frac{\partial \varepsilon}{\partial x} \frac{\partial v_t}{\partial x} + \frac{\partial \varepsilon}{\partial y} \frac{\partial v_t}{\partial y} \right)$$

$$\Lambda_{\varepsilon} = C_{1\varepsilon} \frac{\varepsilon}{k} \Lambda_k - C_{2\varepsilon} \frac{\varepsilon^2}{k} \quad (2.52)$$

It should be noted that the treatments of the convection terms for the momentum equations, and k and ε equations are different. In the difference equations for the k and ε equations, the upwind difference for convection terms does not take the average of velocity as shown in Eqs. (2.44), (2.45), (2.50) and (2.51), because the velocity component is always located between the related k and ε nodal points.

Pressures in the turbulent regime are in the same form as that in the laminar flow, except that the laminar velocities are replaced by the turbulent mean velocities and the last term I_x and I_y in Eqs. (2-36) and (2-37) are replaced by τ_x and τ_y , respectively.

2.4 INITIAL AND BOUNDARY CONDITIONS

As far as the initial and boundary conditions are concerned, one must be cautious not to violate the law of conservation of mass. In most cases, our main interest is to predict the flow field at steady-state for a specified flow regime. Therefore, the convergence from the initial condition to the stable situation or steady-state should be as fast as possible. With these considerations in mind, the present study introduces the initial conditions as:

$$\left. \begin{aligned} U(x,y,t) &= U(y) \\ V(x,y,t) &= 0. \end{aligned} \right\} \text{ at } t=0 \quad (2.53)$$

For the boundary conditions, the upper and lower walls are non-slip type. The inlet and outlet conditions are defined so that the U-velocity gradients with respect to x are zero. In the expressions of nodal variables, the boundary conditions can be written as the following:

$$\begin{aligned} &V_{i,j_{\max}} = 0, \quad V_{i,j_{m-1}} = 0 \\ \text{Upper Wall (non-slip):} \quad &U_{i,j_{\max}} = -U_{i,j_{m-1}}, \quad k_{i,j_{\max}} = -k_{i,j_{m-1}} \\ &\varepsilon_{i,j_{\max}} = -\varepsilon_{i,j_{m-1}} \end{aligned} \quad (2.54)$$

where i_{m-1} and j_{m-1} equal $i_{\max}-1$ and $j_{\max}-1$, respectively.

$$\begin{aligned} &V_{i,1} = 0, \quad V_{i,2} = 0, \quad U_{i,1} = -U_{i,2} \\ \text{Lower Wall (non-slip):} \quad &k_{i,1} = -k_{i,2}, \quad \varepsilon_{i,1} = -\varepsilon_{i,2} \end{aligned} \quad (2.55)$$

$$V_{1,j} = V_{2,j}, \quad U_{1,j} = U_{2,j}$$

Inlet Wall:

$$k_{1,j} = \frac{3}{2}(0.01U_{in})^2, \quad \varepsilon_{1,j} = \frac{C_{\mu}^{3/4} k_{1,j}^{3/2}}{0.03D_{in}} \quad (2.56)$$

where U_{in} is inlet velocity, D_{in} is inlet diameter.

Outlet Wall:

$$\begin{aligned} V_{imax,j} &= V_{im1,j}, \quad U_{imax,j} = U_{im1,j} \\ k_{imax,j} &= k_{im1,j}, \quad \varepsilon_{imax,j} = \varepsilon_{im1,j} \end{aligned} \quad (2.57)$$

The notation of imax, jmax corresponds to the same names as shown in Figure 2.4. It should be noted that the $V_{i,2}$ and $V_{i,jm1}$ are velocities at the lower and upper boundaries of the real domain (the computational domain has fictitious cells on four boundaries). They should be zero as the non-slip condition requires. This is not defined either by Hirt et al. (1975) or Cai (1993). U_{i1} , $U_{i,2}$, $U_{i,jmax-1}$, and $U_{i,jmax}$ are not on the boundaries because of the introduction of the fictitious cells along the boundaries. For pressures, only those on the upper and outlet boundaries are necessary to define, because of the adoption of the forward difference schemes in the pressure derivatives. The numerical values on the upper and outlet boundaries are defined by linear extrapolation as Eqs (2.58) and (2.59), respectively.

$$P_{i,jmax} = P_{i,jm1}. \quad (2.58)$$

$$P_{imax,j} = 2P_{im1,j} - P_{im2,j} \quad (2.59)$$

where im_2 equals $imax-1$. The pressures on the upper and lower boundaries will be updated after each iteration. Such an artificial treatment is based on the velocity definitions

on the upper and outlet boundaries. On the outlet boundary, from the momentum equation, we see that at a defined y , the pressure gradient with respect to x is approximately a constant, because zero transverse velocity and zero axial velocity gradient in the x -direction. The pressure gradient in the x -direction equals the turbulent stress plus the viscous diffusion ($\partial^2 U / \partial y^2$ may not equal zero). Therefore, linear extrapolation in the x -direction is reasonable for the outlet boundary. For the upper boundary, both V and its gradient with respect to y are zero. From the momentum equation in the y -direction, we see that the pressure gradient with respect to y must be zero on the upper boundary. Previous studies (Hirt et al., 1975; Cai, 1993) implicitly assign zero to these values which may have introduced errors in the flow field calculations.

2.5 SOLUTION PROCEDURE AND PRESSURE ITERATION

Because of the nonlinear nature of the equations governing the fluid flow inside and outside of a filter, the solution procedure must be iterative. Velocities are solved first and then pressures are obtained by Eqs. (2-22), (2-23) and (2-34) and equations for the turbulent flow. However, such an iteration cannot bring the velocities to satisfy the continuity equations as given in Eq. (2-21) for laminar flow and Eq. (2-38) for turbulent flow. Up to now, no explanation for such a problem is given in the references, even though the problem has been discovered a long time ago (Hirt et al., 1975). The most popular remedy for this problem is to adjust the cell pressure. The "adjusting the cell pressure method" is used in the SOLA algorithm to obtain better estimated velocities. In this method, the dilatation D is expressed as:

$$D = \frac{U_{i,j}^{n+1} - U_{i-1,j}^{n+1}}{\Delta x} + \frac{V_{i,j}^{n+1} - V_{i,j-1}^{n+1}}{\Delta y} \quad (2.60)$$

The basic theory of this technique is that the pressure gradient between a cell and its ambient cells determines the net inflow or outflow for a cell. If the dilatation D in Eq. (2.60) is negative, the net mass flow is into the cell and increasing pressure is needed to eliminate the inflow. On the other hand, when D is positive, the net mass outflow is compensated by decreasing pressure. The one pressure variable in each cell allows the dilatation D to be driven to an acceptable small value. Since the adjustment of the cell will affect its neighbor cell values, the iteration of the pressure adjustment must be performed throughout the whole flow domain. The dilatation D is calculated by using the most recently updated velocity values. When a cell pressure changes from p to $p+\Delta p$, the velocity components on the four faces of that cell change as:

$$U_{i,j}^{n+1} = U_{i,j}^n + \frac{\Delta t \cdot \Delta p}{\Delta x} \quad (2.61)$$

$$U_{i-1,j}^{n+1} = U_{i-1,j}^n - \frac{\Delta t \cdot \Delta p}{\Delta x} \quad (2.62)$$

$$V_{i,j}^{n+1} = V_{i,j}^n + \frac{\Delta t \cdot \Delta p}{\Delta y} \quad (2.63)$$

$$V_{i,j-1}^{n+1} = V_{i,j-1}^n - \frac{\Delta t \cdot \Delta p}{\Delta y} \quad (2.64)$$

Substituting these equations into the continuity equation will yield the required difference pressure form:

$$\Delta P = -\omega \cdot D / \left\{ 2\Delta t \left(\frac{1}{\Delta x^2} + \frac{1}{\Delta y^2} \right) \right\} \quad (2.65)$$

Where ω is an over-relaxation factor introduced to accelerate the iteration convergence. The value of ω is chosen as 1.7 in this study. It should be noted that the ΔP is just the net pressure difference between the concerned cell and its ambient cells, assuming that the pressures are the same for the ambient cells. It is obvious this is not true for most flows. However, the velocity calculation is an iterative process. The ΔP calculation will sweep the whole computational domain. Therefore, the assumption may be valid. In the pressure iteration, the dilatation D is evaluated first, then ΔP and finally velocities are updated as in Eqs. (2.61) to (2.64). Considering these equations carefully, we will find that they are new forms of the momentum equations with the neglect of convection and diffusion terms ($\partial U/\partial t = \pm \partial P/\partial x$ and $\partial V/\partial t = \pm \partial P/\partial y$).

2.6 NUMERICAL STABILITY CONSIDERATIONS

The choice of grid size Δx and Δy , time increment Δt , and upstream difference parameter α will affect both the numerical solution and the stability. The grid size should be reasonably small in order to yield reasonably accurate results. However, the exact value of the grid size depends on both the flow regime and the dimension of the computational domain. In high Reynolds number flow regimes, the grid size should be smaller than that in low Reynolds number regimes. Furthermore, if the computational domain is large and the velocity of the flow is low, a relatively large grid size can be utilized. Once the mesh space is determined, the choice of the time increment must satisfy the following two conditions

(after Hirt et al., 1975): First, fluid cannot move more than one cell size for the given time step. This leads to the inequality:

$$\Delta t_1 < \min \left\{ \frac{\Delta x}{|U|}, \frac{\Delta y}{|V|} \right\} \quad (2.66)$$

Second, the non-zero value of kinematic viscosity requires that the momentum diffusion cannot be over one cell size in the given time step. Then the following condition must be satisfied (after Hirt et al., 1975):

$$\nu \cdot \Delta t_2 < \left\{ \frac{1}{2} \frac{\Delta x^2 \Delta y^2}{\Delta x^2 + \Delta y^2} \right\} \quad (2.67)$$

Note that the dimension of the kinematic viscosity, ν , is m^2/s . Therefore, the left and right hand sides of the inequality (2.67) have the same dimension. The Δt is chosen as the minimum value of those two criteria: $\Delta t = \min\{\Delta t_1, \Delta t_2\}$. Furthermore, inequalities (2.66) and (2.67) imply that the convection and diffusion of the fluid flow must be confined within a cell. This is actually a physical limitation for the difference equation. However, these physical limitations do not guarantee the numerical stability and accuracy. In practice, it is found in this study that to maintain both the stability and accuracy, Δt should be approximately 100 times smaller than the minimum of the criteria derived from inequalities (2.66) and (2.67). This number (100 times) is obtained by trial and error. After a systematic decrease of Δt , which must be smaller than the stability criteria, we will find a converged solution, i. e. the discrepancy between solutions of two successive runs is

negligible. This negligible discrepancy can be defined based on various situation and the requirement of the accuracy. In this study, it is observed that the discrepancy is less than 1% of the maximum velocity when the time step is 100 times less than the stability criterion.

The upstream difference coefficient α applied to the convection terms of the momentum equation also has to satisfy the condition:

$$1 \geq \alpha \geq \max \left\{ \left| \frac{U\Delta t}{\Delta x} \right|, \left| \frac{V\Delta t}{\Delta y} \right| \right\} \quad (2.68)$$

The value of α should be in the range 0 to 1. The case of α equal to 0 is equivalent to the central difference and 1 refers to the fully upwind or donor cell difference. In this study, 0.8 is used for the α .

2.7 RESULTS AND DISCUSSION

For a defined computational domain as given in the present study, several factors such as, fluid properties (density and viscosity), and the characteristics of the medium (texture, porosity, permeability), through which fluid flows, can affect the fluid flow. In this study, attention is mainly paid to the following three aspects: 1) the effects of the grid size and time step Δt on the accuracy of the solution and the elapsed time for the flow to reach the steady-state condition; 2) the effects of the thickness of the filter; 3) the effects of the permeability of the filter. The constants used in the modeling study are listed in Table 2.2.

Explanations	Code names	Values	Units
Maximum axial inlet velocity	Ui	3.0	m/s
Transverse inlet velocity	Vi	0.0	m/s
Cell number in x-direction	ibar	42	
Cell number in y-direction	jbar	20	
Dynamic viscosity of the air	nu	1.453e-5	N•s/m ²
Density of the air	rol	1.201	kg/m ³
Over-relaxation factor	alpha	1.7	
Gravitational acceleration in x, y	gx, gy	0	m/s ²

Table 2.2 Constants used this study, where the code names are consistent with those in the program TLUV2D.

2.7.1 The Effects of Grid Size and Time Step on Velocity Changes

Several tests with various grid sizes and time steps have been conducted in order to understand the pattern of the velocity variation with time, namely, velocity evolution. These tests, by and large, fall into two groups. In the first, the grid size is defined and the magnitude of the time step is allowed to change. In the second group, the magnitude of the time step is maintained constant and the grid size is varied. The results from the first group are illustrated in Figure 2.6 for the velocity variation at the geometrical center of the filter. In this test, a constant grid size of 0.1 m and a uniform K of 10^{-4} m^2 are used. The time step varies from 5.0×10^{-6} to 10^{-4} s.

From Figure 2.6, we see that the general pattern of the U-velocity evolution in terms of the rate of change is the same for various lengths of time steps. There is a rapid decrease during the first millisecond (ms) which is followed by slow changes. After 3 ms the velocity changes with time are negligible. This indicates that the flow regime will reach a steady-state after 3 ms of elapsed time. The test also indicates that the time step Δt has a significant effect on the solution of the velocity field. In particular, as Δt is larger than 10^{-5} s, the results may have large discrepancies from the converged solutions. However, when the Δt is smaller than 10^{-5} , the difference in the velocity evolution will be negligible. Therefore, it seems that the Δt of 10^{-5} s is a good choice for the defined flow regime. In the execution of the computer program TLUV2D, a parameter must be provided. This parameter is a time factor, which is used to multiply the Δt calculated from the stability criterion. The time factor must be less than 1.0. In cases presented in Figure 2.6, the

stability criterion is 10^{-3} s. Therefore, the best choice of time step, Δt , 10^{-5} is 100 times smaller than the stability criterion.

The effects of the grid size with a constant time factor of 100 are depicted in Table 2.3, because the U-velocity discrepancies for the different grid sizes are too small to be visualized in a figure. From this table, we see that the solutions of the velocity at the center of the filter are independent of the grid size within the range from 0.01 to 1.0 m.

From the tests for the effects of the grid size and time step on the velocity evolution, it may be concluded that an increase of the time step can cause inaccuracy of the solution and a Δt of 10^{-5} s which is 100 times smaller than the stability criterion, seems to be appropriate. The grid sizes within the range from 0.01 to 1.0 m virtually give the same result for a Δt of 10^{-5} s. Therefore, when the computational domain becomes large, we may use large grid size while maintaining an appropriate time step.

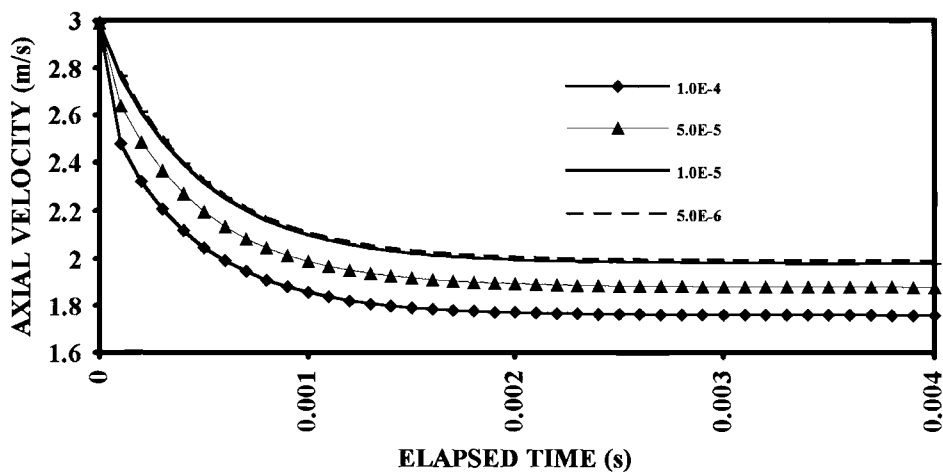


Figure 2.6 The effect of the time step on the solution of the axial velocity at the center of the filter with uniform K and Δx equal to 10^{-4} m² and 0.1 m, respectively. The numbers in the legend are Δt (in seconds).

TIME (s)	$\Delta x=1.0\text{m}$	$\Delta x=0.1\text{m}$	$\Delta x=0.01\text{ m}$
0.0000	2.9925	2.9925	2.9925
0.0001	2.7664	2.7664	2.7664
0.0002	2.6125	2.6125	2.6126
0.0003	2.4910	2.4910	2.4911
0.0004	2.3938	2.3938	2.3939
0.0005	2.3156	2.3156	2.3158
0.0006	2.2525	2.2525	2.2527
0.0007	2.2015	2.2015	2.2017
0.0008	2.1601	2.1601	2.1603
0.0009	2.1266	2.1266	2.1268
0.0010	2.0993	2.0994	2.0995
0.0011	2.0772	2.0772	2.0774
0.0012	2.0592	2.0593	2.0594
0.0013	2.0446	2.0446	2.0447
0.0014	2.0328	2.0328	2.0328
0.0015	2.0231	2.0231	2.0231
0.0016	2.0152	2.0152	2.0152
0.0017	2.0088	2.0088	2.0087
0.0018	2.0036	2.0035	2.0034
0.0019	1.9993	1.9993	1.9991
0.0020	1.9958	1.9958	1.9956
0.0021	1.9929	1.9929	1.9927
0.0022	1.9906	1.9906	1.9903
0.0023	1.9887	1.9886	1.9883
0.0024	1.9871	1.9870	1.9867
0.0025	1.9858	1.9857	1.9854
0.0026	1.9847	1.9846	1.9843
0.0027	1.9838	1.9837	1.9833
0.0028	1.9830	1.9830	1.9826
0.0029	1.9824	1.9823	1.9819
0.0030	1.9819	1.9818	1.9814
0.0031	1.9814	1.9814	1.9809
0.0032	1.9810	1.9810	1.9805
0.0033	1.9807	1.9806	1.9802
0.0034	1.9804	1.9804	1.9799
0.0035	1.9802	1.9801	1.9797
0.0036	1.9799	1.9799	1.9795
0.0037	1.9798	1.9797	1.9793
0.0038	1.9796	1.9796	1.9791
0.0039	1.9794	1.9794	1.9790
0.0040	1.9793	1.9793	1.9789

Table 2.3 Velocity changes with time with at the geometrical center of the filter with a uniform permeability, K , 10^{-4} m^2 and Δt 100 times smaller than the stability criterion.

The convergence of numerical solutions is restrained by two criteria. The first is the dilatation factor, D , which ensures the continuity will not be violated. In this study, it is observed that the maximum D is less than 10^{-4} when the iteration is over 500 times. Therefore, the number of iterations is set to be 1000 to maintain the accuracy of the solution. The second criteria for convergence is the relative error, which is defined as the ratio of the maximum discrepancy between two successive runs to the maximum velocity. It is found in the present study that the relative error is less than 1% when the time factor is 100, i.e. the time step Δt is 100 times less than the stability criterion. In summary, at each time step, 1000 iterations were performed to insure convergence at all grid points. The time was then stepped forward by Δt . The process was continued until a steady state was reached at an elapsed time of 3 ms.

A uniform grid size of 10 mm, 42 and 20 cells in x- and y-direction, respectively, are used to obtain results presented in the following subsections. All results about the velocity distribution are assumed to be at steady state, i.e. the elapsed time is 3 ms as discussed earlier in this section.

2.7.2 General characteristics of the flow fields with uniform K

As initially defined, a fully developed turbulent flow passes through a filter medium where laminar flow prevails, and the flow downstream of the filter is turbulent. Several tests are made with uniform distribution of K and the results are presented in Figures 2.7 and 2.8. The flow regimes in the given computational domain demonstrate the following characteristics:

- In the regions upstream of the filter, as the flow approaches the filter, the axial velocity decreases rapidly and the flow diverges about the center line;
- Within the filter, a uniform velocity field is observed at the central area of the filter. The velocity gradient du/dy must be large near the lower and upper boundaries of the domain, because of the no-slip condition imposed on both lower and upper boundaries;
- In the regions downstream of the filter, as the flow leaves the filter, it converges rapidly. The velocity profiles along the x-axis change from a flat to an approximately fully-developed profile.

The pressure distributions in the x-direction for the case of uniform permeability distribution are depicted in Figure 2.9. The pressures are almost constant in the regions upstream and downstream of the filter. When K is lower than 10^{-6} m^2 , the difference between pressure drops for different K appears negligible. However, as K values decrease from 10^{-6} to 10^{-8} m^2 , the pressure drop increases significantly. These results do not agree with one-dimensional analysis and require further study. These results suggest a drastic change in the velocity field and pressure drop will occur as K is lower than the critical value of 10^{-6} m^2 . Furthermore, the linear nature of the pressure drop along the center of the filter in the x-direction seems to indicate that the effects of the inertial forces on fluid flow and viscous dissipation in the filter are not significant. This linearity was also observed by Cai (1993).

Pressure measurements in the SAE J726 test housing show that the pressure drop across a clean automotive panel air filter is about 360 Pa ($\text{N}\cdot\text{m}/\text{s}^2$). This pressure drop corresponds to a permeability of about 10^{-4} m^2 . This permeability is very high compared with Tebbutt's (1995) experimental results. Tebbutt conducted a series of pressure measurement experiments across flat filter paper mounted in a pipe. He obtained a permeability of $8.16 \times 10^{-11} \text{ m}^2$ for a single layer of filter paper. It should be mentioned that the permeability of porous medium is the property of the medium, i.e. it does not depend on the shape or dimensions of the medium. It is anticipated that the permeability of the flat filter paper and the pleated filter made of the same fibrous paper should be the same. The reason for such a huge difference between predicted and measured pressure drops is not clear at this stage. The ΔP corresponding to a full design capacity of the automotive filters is about 2500 Pa. According to the modeling result (Figure 2.9), the permeability of a full capacity filter should be less than 10^{-8} m^2 . The permeability of dirty filter should be documented in the future.

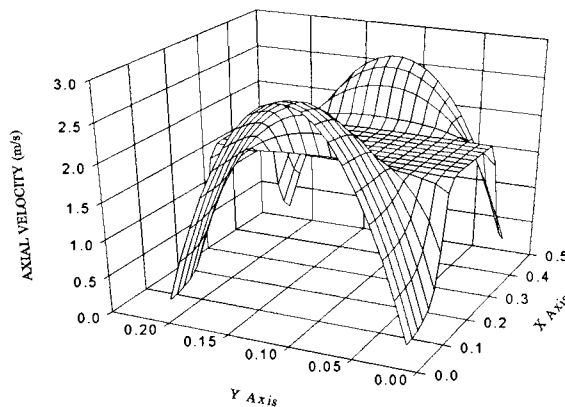


Figure 2.7 Axial velocity distribution in the computational domain with K and grid size equal to 10^{-4} m^2 and 0.01 m, respectively.

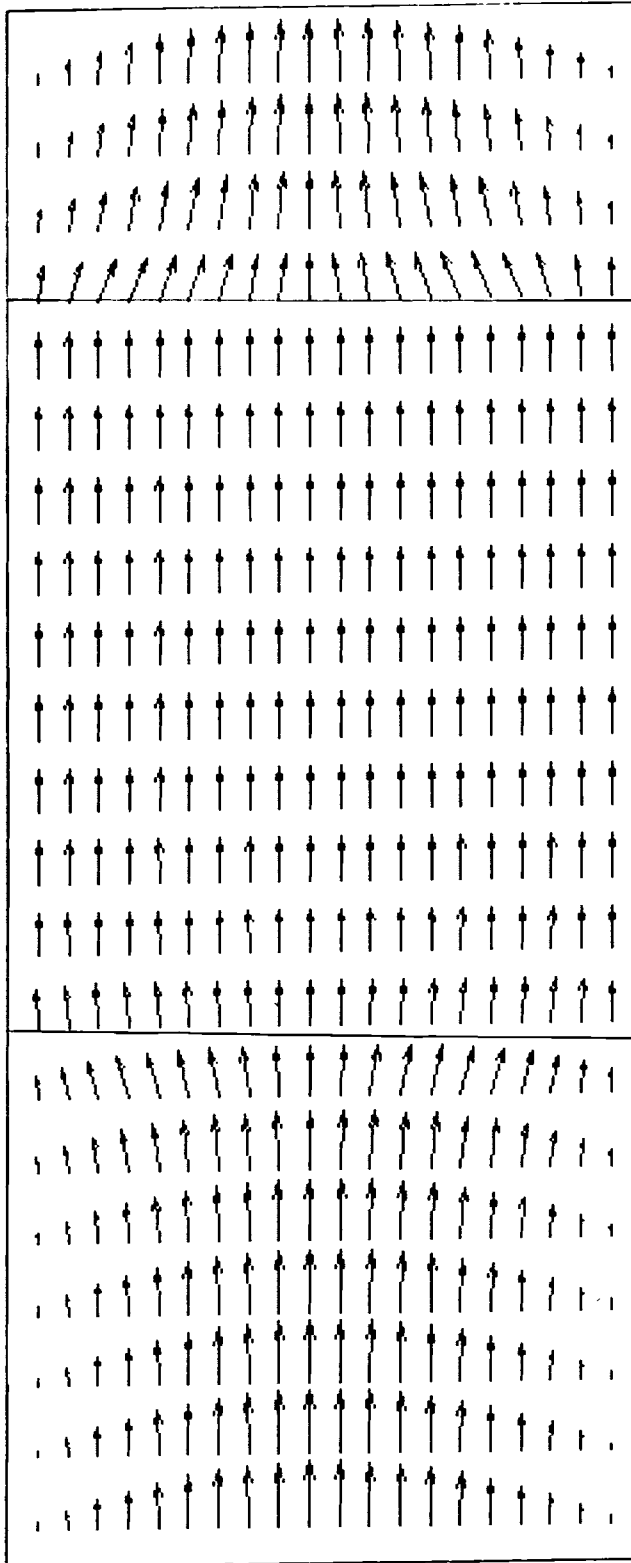


Figure 2.8 The velocity field for a uniform K of 10^{-4} m^2 and grid size of 0.01 m .

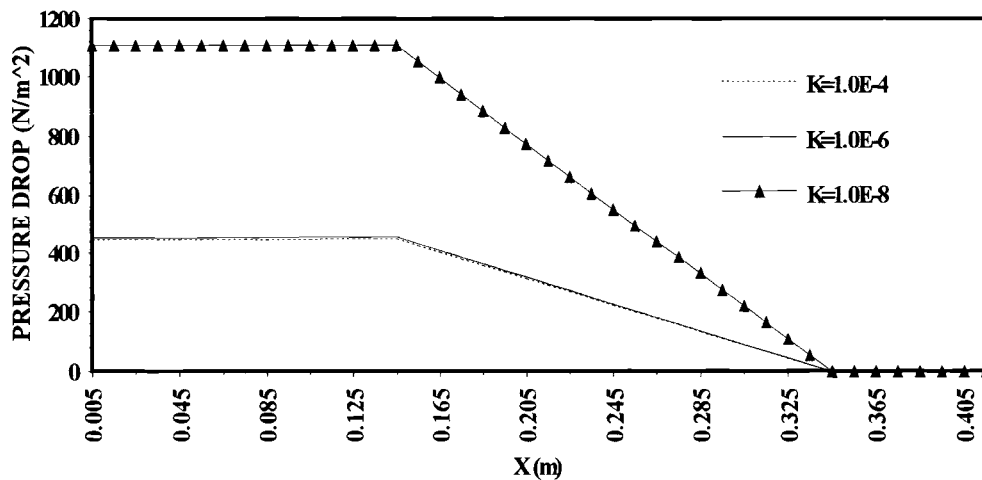


Figure 2.9 Pressure distribution along the center-line of the filter, where K in the legend is the permeability (in m^2).

The changes in K can slightly alter the velocity distribution, as shown in Figure 2.10. The higher the K, the larger the axial velocity at the center of the filter and lower in the area near the walls. However, these differences are almost negligible for the uniform distribution of K. Such a pattern of velocity distribution is due to the confinement of the flow domain, i.e. to maintain continuity, the velocity profile at a specific x must be similar in shape (here the ‘similar’ does not mean that the velocity profiles have a similarity solution). The same explanation applies to the effect of the filter thickness on the velocity fields. As shown in Figure 2.11 where d is equal to 0.1 m, the velocity field is almost the same as for d equal to 0.2 m. However, if the K is not uniformly distributed in the filter, the fluid will flow faster in the area where K is large, and the resistance to flow is small.

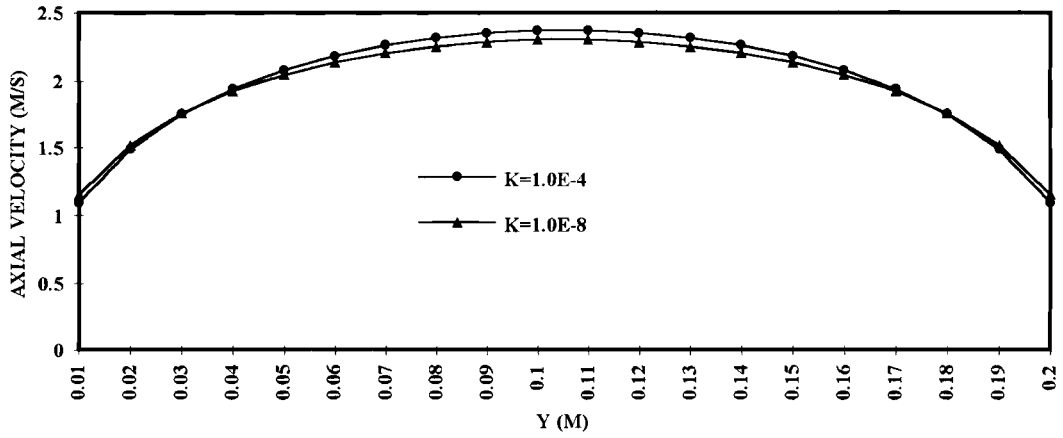


Figure 2.10 A comparison of the axial velocities at x equal to 0.13 m for different K (in m^2). The filter is located between x equal to 0.15 and 0.20 m.

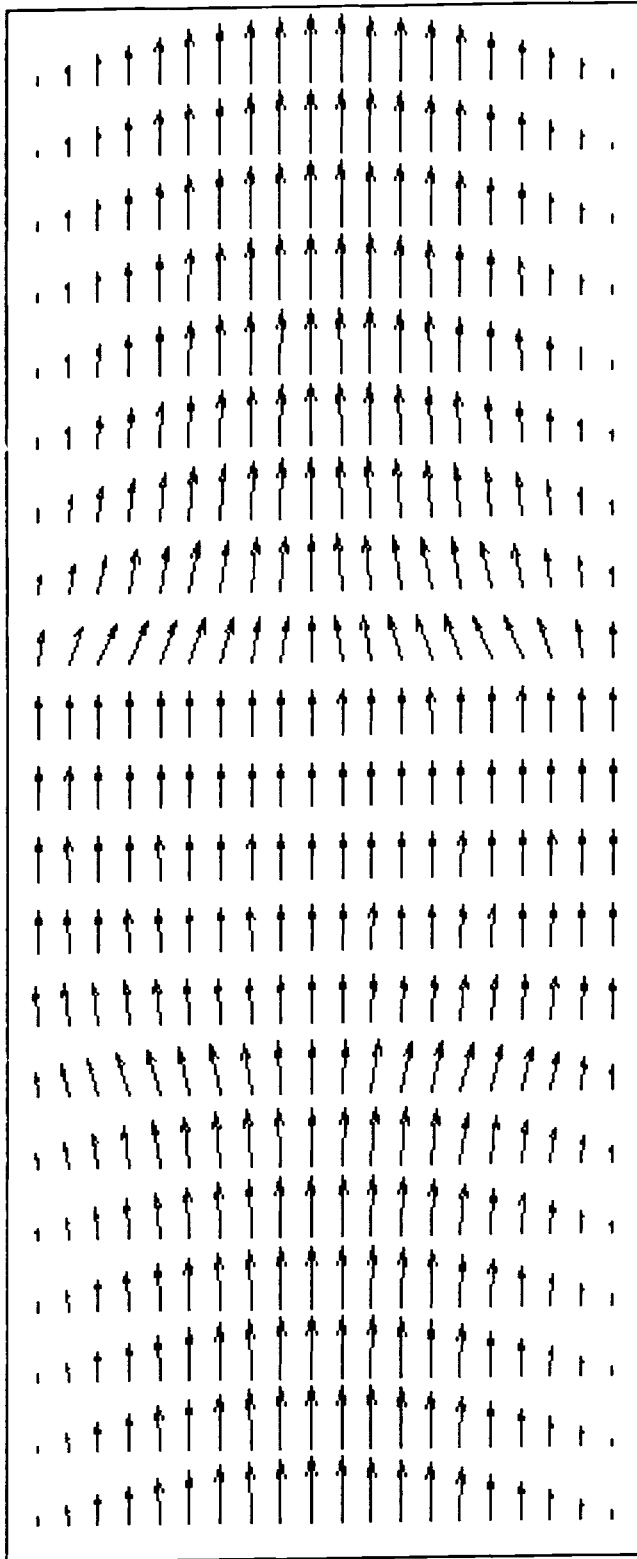


Figure 2.11 The flow field with K equal to 10^{-6} m^2 and d 0.1 m.

2.7.3 Effects of the inhomogeneity of the K

Dust loading on an automotive air filter is an unavoidable process, and such dust loading is most probably not uniform, because of the complex distribution of the velocity field upstream of the filter as documented by Gurumoorthy (1990), Newman (1994), and Duran (1995). Understanding of the effects of the magnitude and distribution of K on the velocity redistribution upstream of an automotive filter are important to the enhancement of dust holding capacity and filtration of a filter.

Several situations with respect to the inhomogeneity of the K in the filter have been considered in this study. The first is that one-fifth of the filter (in the y -direction) with K of 10^{-8} m^2 is located at the center of the filter and K of 10^{-6} m^2 for the rest of the filter. The velocity distribution is illustrated in Figure 2.12. For this kind of K distribution, we see that the divergence and convergence upstream and downstream of the filter have the same characteristics as in the case of uniform K . The difference is that the axial velocity at the center of the filter is significantly decreased. The axial velocity profiles at x equal to 0.15 m, the upstream boundary between the filter and the turbulent flow regime, are shown in Figure 2.13, where K equals 10^{-8} m^2 at the central strip and 10^{-6} and 10^{-7} m^2 for the rest of the filter for the triangle and circle-marked line respectively. From this figure, we see that for the cases with the same permeability, K , at the central strip and varied K near the wall strips, the axial velocity at the center of the filter will be slightly higher for the low value of K near the wall strips, because of the confinement of the air induction system.

The second test conducted with respect to the inhomogeneity of K is to assign a K of 10^{-8} m^2 for the left half of the filter and K of 10^{-6} m^2 for the other half. The velocity field as shown in Figure 2.14 demonstrates a similar characteristic to the uniform K of 10^{-8} m^2 , except that the convergence downstream of the filter seems to be stronger than that for the uniform K . Here the axial velocities are not symmetrical about the center of the filter as shown in Figure 2.15, where the decrease upstream of the filter is faster than the increase downstream of the filter.

The permeability distribution for the third test is illustrated in Figure 2.16. The filter is divided into 6 zones. The permeability in each zone is assigned as follows: Zone 1: $K_x=10^{-6}$, $K_y=10^{-7}$; Zone 2: $K_x=10^{-8}$, $K_y=10^{-8}$; Zone 3: $K_x=10^{-6}$, $K_y=10^{-7}$; Zone 4: $K_x=10^{-8}$, $K_y=10^{-7}$; Zone 5: $K_x=10^{-6}$, $K_y=10^{-8}$; Zone 6: $K_x=10^{-8}$, $K_y=10^{-7}$. It should be mentioned that the program allows K to have different values in the x - and y -directions, a characteristic that is frequently encountered in porous media. However, in our computations, the y -component of K has very small effects because of the low values of transverse velocity V . The velocity distribution for the six-zone filter is illustrated in Figure 2.17. We see that there are two converging zones. One occurs at the center (in the x -direction) of the filter and the other occurs downstream of the filter.

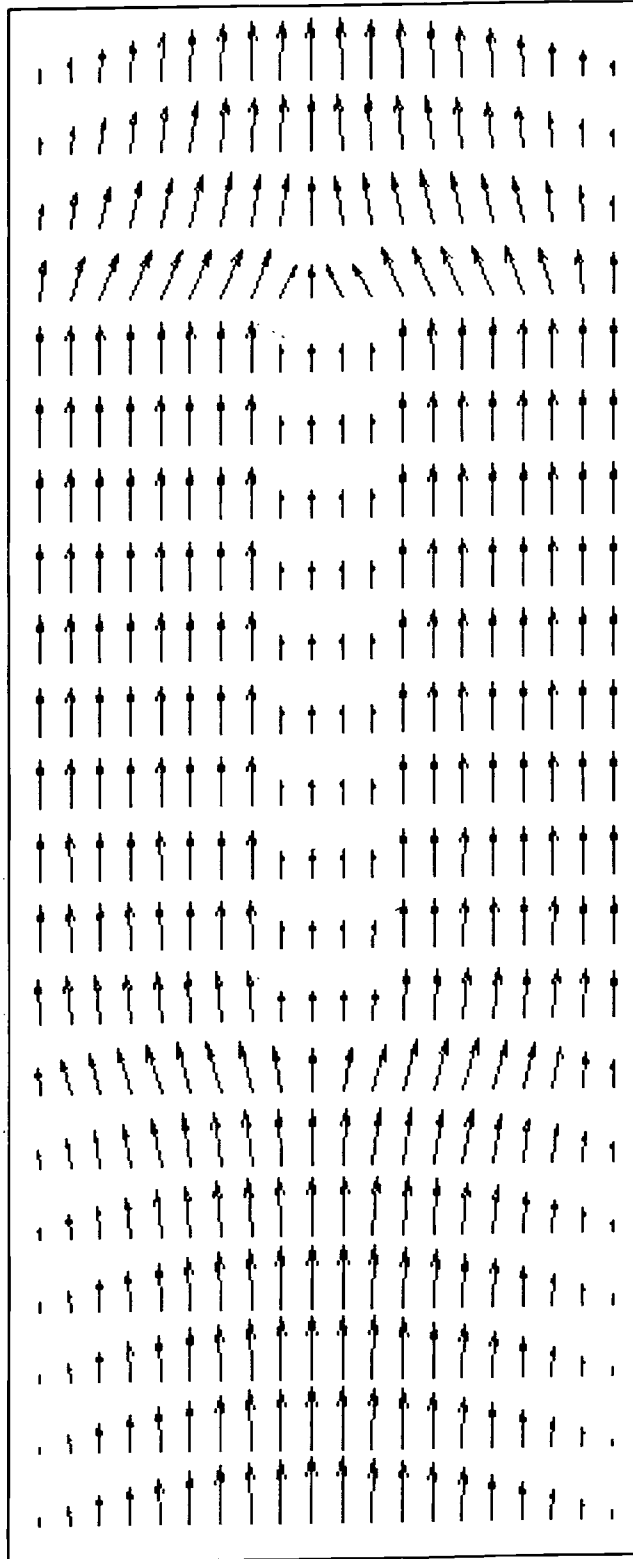


Figure 2.12 The flow field for K equal to 10^{-8} m^2 at the central strip (0.04 m) and 10^{-6} m^2 for the rest of the filter.

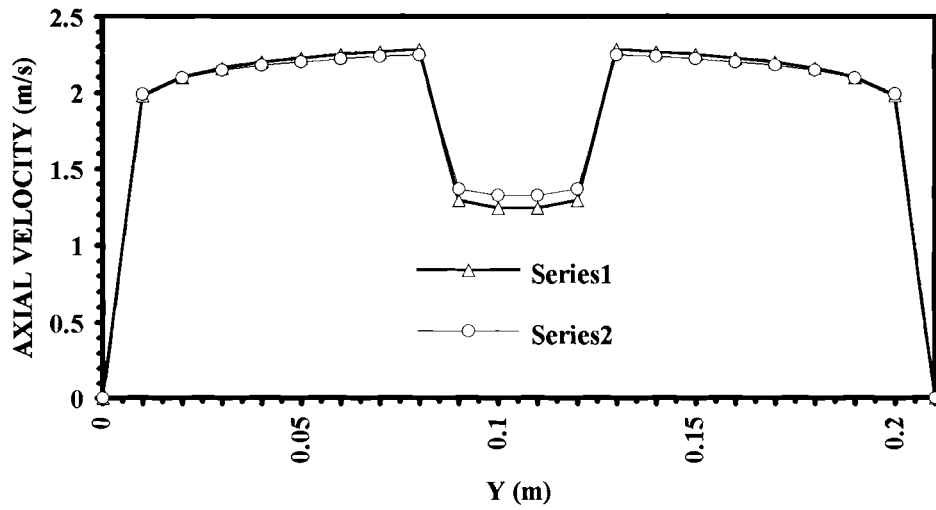


Figure 2.13 A comparison of the axial velocity at x equal to 0.15 m. The filter is located between 0.15 and 0.20 m. K equals 10^{-6} m^2 (for Series 1) and 10^{-7} m^2 (for Series 2) outside the core area, and 10^{-8} m^2 at the core area (for both Series 1 and 2).

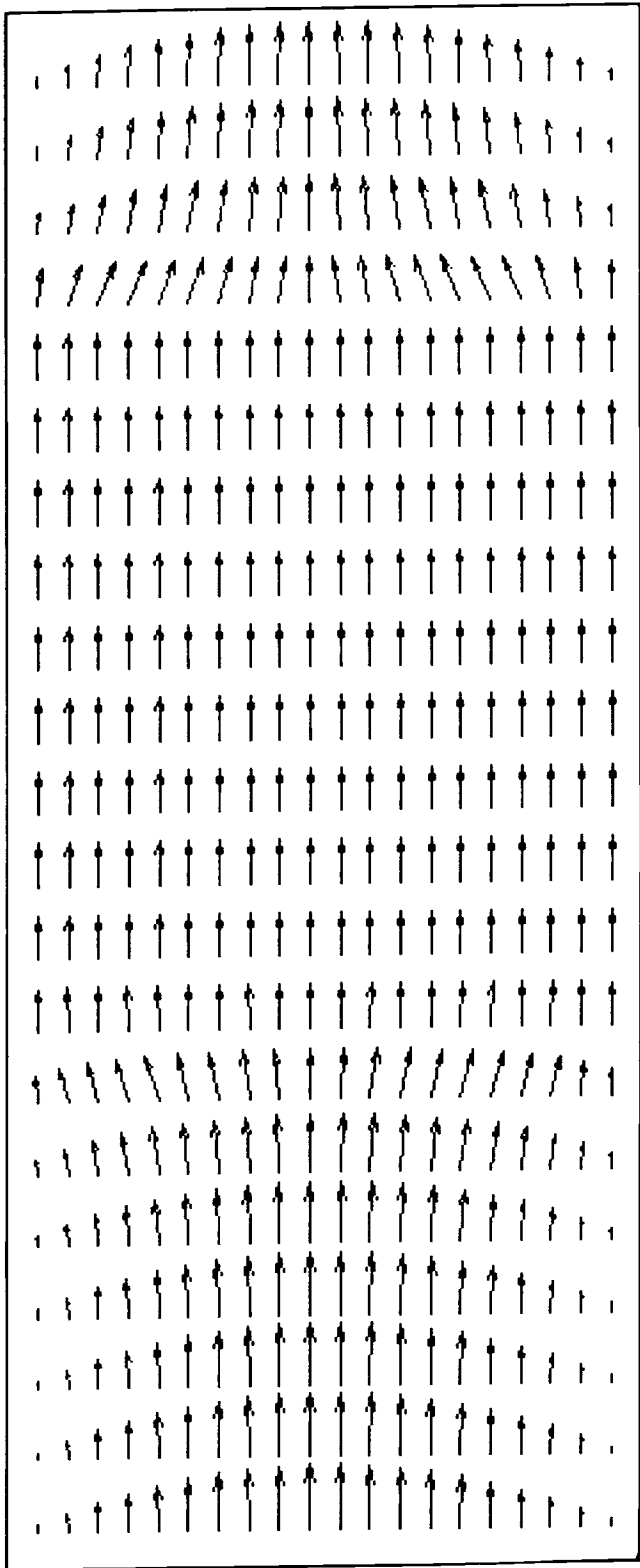


Figure 2.14 Velocity field with $K=10^{-8}$ and 10^{-6} m^2 for the left half and right half of the filter, respectively.

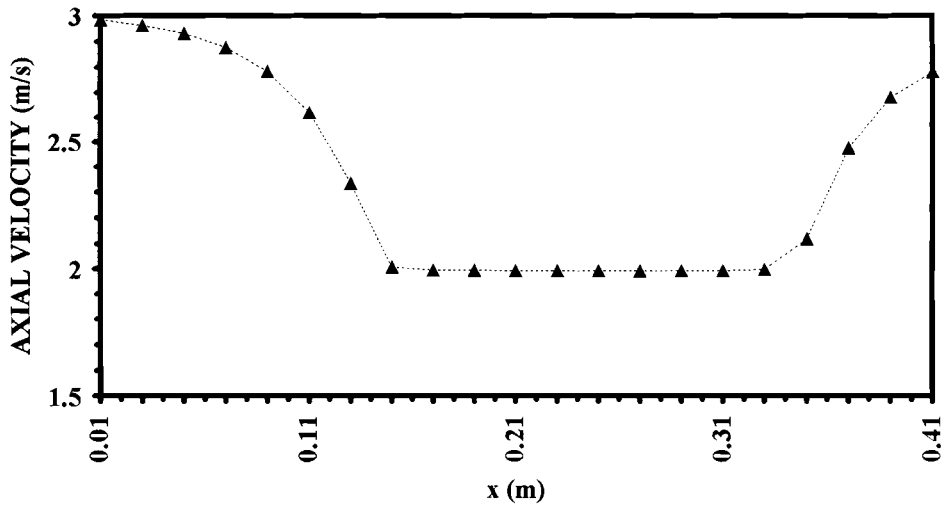


Figure 2.15 The axial velocity distribution at y equal to 0.1 m (the center in the y-direction) with non-uniform distribution of K in filter.

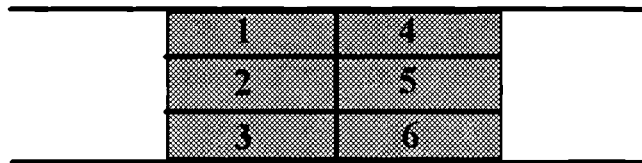


Figure 2.16 The distribution of permeability in the filter where the number is the zone number.

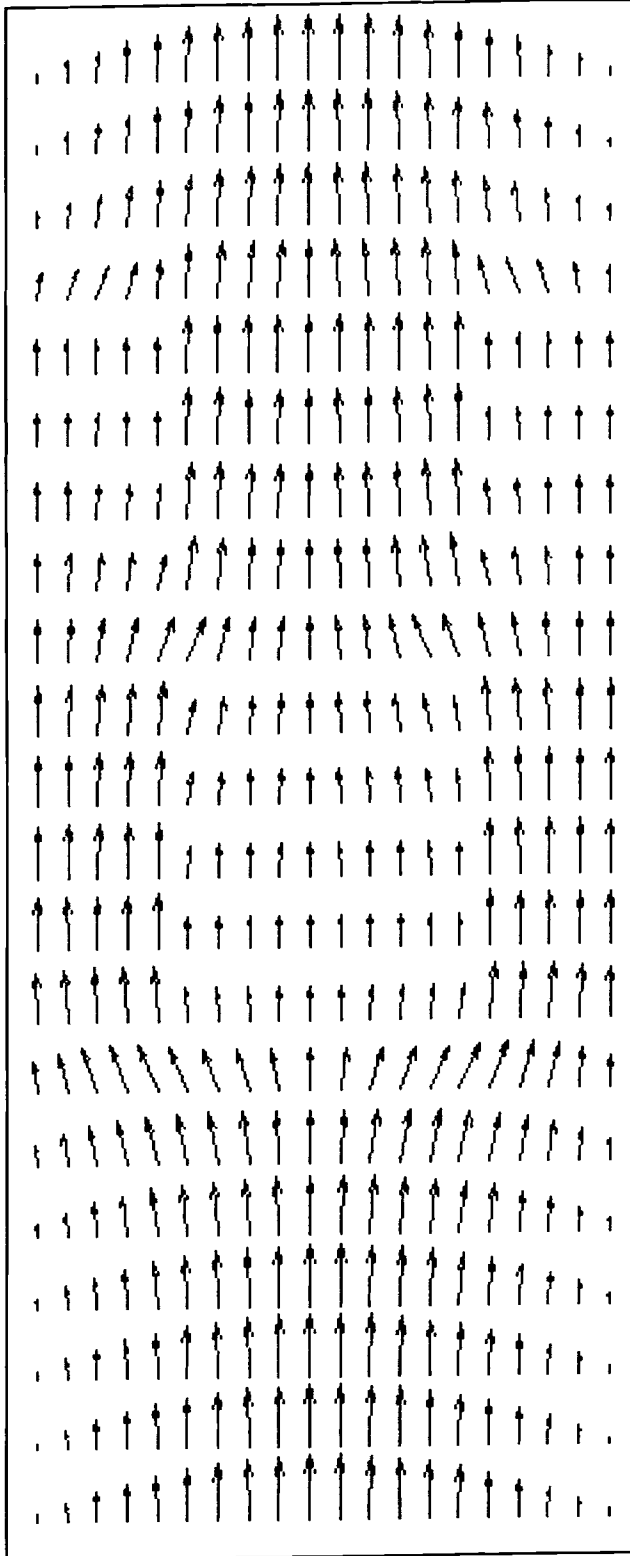


Figure 2.17 The velocity field with K distribution as shown in Figure 2.16.

2.7.4 Discussion

Two problems encountered in this study need to be stressed. The first is related to the algorithms for solving Navier-Stokes equations and the second concerns the input parameters K and b . Both are of importance in obtaining the solution of the velocity field and pressure drops when a steady-state flow regime is achieved.

In the implementation of the numerical algorithm to obtain U , V , and P by solving the Navier-Stokes and continuity as well as the k - and ε -equations, initially, the pressure distribution is unknown. It is obtained by solving the momentum equations for the filter region, and a combination of momentum and k - ε equations for the region outside the filter. The problem is that continuity cannot be satisfied, if we solve momentum and continuity equations for pressure directly. This was noticed by Hirt et al. (1975) and Ramaswamy (1990). In order to satisfy continuity, Eqs (2.60)-(2.65) were introduced.

Theoretically, these equations presume zero diffusion and convection. This is obviously not the case. Practically, this treatment works well. On one hand, after several iterations by directly using the N-S and continuity equations, the solution should approach the real solution. However the precision is not good enough because of the high nonlinearity. The pressure iteration forces continuity and works more efficiently for each advance of Δt . On the other hand, to justify the pressure difference Δp for each cell to force the net inflow equal to net outflow, physically, does make sense, because the pressure difference between the considered cell and its ambient cells dominantly controls the inflow and outflow.

For the CFD modeling of the fluid flow in a porous medium, the most important factors are probably permeability K and inertial factor b . Tebbutt (1995) determined the K and b for the filter paper by experimental methods. He mounted a piece of flat filter paper at the center of a 12 m long and 7.62 cm in diameter pipe, and measured the change in pressure drop across the paper at different flow rates. Equation (2.69) was used in order to determine K and b by linear regression.

$$\Delta P = \frac{\mu}{K} \left(\frac{Q}{A} \right) + \frac{b\rho}{2} \left(\frac{Q}{A} \right)^2 \quad (2.69)$$

Q is volume flow rate and A is the area of the cross section of the pipe. Note that Q/A is the average velocity. b is the inertial factor and ρ is the density of the air. Note that the first and second terms in Eq. (2.69) are Darcy's law and the inertial forces, respectively. Linear regression can be used to obtain the corresponding K and b . The viscous dissipation term is not included in Eq. (2.69). The consequence of such a neglect of viscous dissipation is not known. Tebbutt obtained the numerical values of K and b equal to $8.16 \times 10^{-11} \text{ m}^2$ and $6.79 \times 10^4 \text{ m}^{-1}$, respectively, for a single layer of filter paper. Both values are independent of the thickness of the porous media. Therefore, it seems that K and b are properties of the porous media. It is well known that K is the property of the porous media which determines the resistance to the fluid flow. Panda and Lake (1994), using the modified Carman-Kozeny equation, concluded that K can vary from 10^{-12} to 10^{-5} m^2 for uniformly packed particles with a diameter of $100 \text{ }\mu\text{m}$, and permeability is purely dependent on the porosity of the media. However, K not only depends on the porosity, but also on the tortuosity, the property of the interconnected pore system. The inertial factor,

b, is less known. In this study, the b is a constant of 1147 m^{-1} which was used by Gurumoorthy (1990) and Cai (1993). This value of b is almost 6 times smaller than that, 6.79×10^4 , obtained by Tebbutt (1995).

If Tebbutt's estimate of the permeability of a single layer filter paper is reasonable, the permeability of dirty filters must be much lower than $8.16 \times 10^{-11} \text{ m}^2$, because of the dust deposition. However, this value seems to be unrealistic according to Panda and Lake (1994). Panda and Lake showed that, when the permeability is smaller than 10^{-12} m^2 , the porosity of the porous medium is less than 10%. Of course, the permeability is not only dependent of permeability, but also of the tortuosity of the porous medium. The microscopic photograph of the filter paper indicates that the porosity of the paper is at least 50% (Natarajan, 1995). If Tebbutt's results are reliable, the tortuosity of the filter must be very small. Much work still needs to be done.

2.7.5 Conclusions

Through this study, with respect to the development of the algorithms, effects of K, Δt and grid size on the velocity distribution and evolution, the following conclusions can be drawn:

- The CFD algorithm allows the grid size to vary from millimeters to a few meters with a time step less than 100 times smaller than the stability criterion. Δt can have a significant effect on the accuracy of the solution. However, it seems that the numerical solution is insensitive to the grid size provided that Δt is in the appropriate range.

- For an initially fully-developed U-velocity profile, the flow takes approximately 3 ms to reach steady-state and this time period seems independent of Δt and grid size.
- Very small pressure drops occur in the turbulent flow regions outside the filter. Significant linearly dropping pressures are observed within the filter along the x-axis as predicted from Darcy's law. This result may indicate that the inertia forces on the fluid flow and the viscous diffusion are insignificant for the cases of the present study.
- The inflow with fully-developed U-velocity profile will be significantly flattened as the flow approaches the filter. Within the filter, the velocity gradients near the wall are very large. This may indicate that the viscosity plays a relatively unimportant role.
- The permeability distribution can significantly alter the flow pattern. Therefore, the present study suggests that to vary the permeability is an important measure to control the velocity distribution upstream of an automotive air filter.

CHAPTER 3

EFFECTS OF THE DUST LOADING ON FILTER INLET VELOCITY REDISTRIBUTION

ABSTRACT

It is the automotive filter designers' desire to produce air filters that will have a uniform velocity distribution upstream of the filter, and consequently, will have dust uniformly deposited. Thus, the filtration efficiency and life span of the filter may be enhanced. However, previous laser Doppler anemometer velocity measurements have shown that clean engine air filters are presented with very non-uniform velocity distributions when tested in the SAE universal panel filter test housing. The effects of the quantities of the dust in an air filter on the velocity distribution have not been quantified previously. The main objective of the present study to develop a qualitative understanding of the effect of the dust loading on the filter and the resulting increase in local flow resistance on the velocity distribution upstream of the filter. In particular, the velocity redistribution upstream of a filter as terminating pressure drop ranges 50% to 150% of the full design terminating pressure drop of 0.254 m of water. Experiments were conducted to measure the changes that occur in this velocity distribution as the filter is loaded with dust. Laser Doppler anemometer measurements of velocity profiles were performed for a production engine air filter in the SAE universal panel filter test housing. Test conditions

Laser Doppler anemometer measurements of velocity profiles were performed for a production engine air filter in the SAE universal panel filter test housing. Test conditions corresponded to a clean filter, filters with 50%, 100%, and 150% of the full design terminating pressure drop.

The results showed that dust loading does make the velocity profiles less non-uniform; the peak, impinging jet-like velocity profiles are broadened. Velocity profiles for the design capacity filter remain very non-uniform. The results obtained from this experiment may have implications for the performance of filters installed in vehicle housings. The results suggest that the velocity distribution presented to filters installed in a vehicle will not change dramatically as the filter accumulates dirt during engine operation. The more gradual changes of the velocity field from peaked, impinging jet-like to a flatter type as the dust capacity increases may indicate the preferential deposition of the dust at the center of the filter, as the dust loading at the center of a filter will increase the resistance, and consequently, the magnitude of the velocities at filter center will decrease.

3.1 INTRODUCTION

Automotive filters are designed to remove dust from the air passing through the air induction system of automobiles. Naturally, improving the understanding of the patterns of the dust distribution inside or on the air filters and the effects of the dust distribution on the velocity distribution of the air flow is of practical interest to the automotive industry. It is believed that such an understanding will be helpful in automotive filter design. Consequently, the dust holding capacity will be increased; filtration efficiency will be improved, and the life span of air filters will be prolonged. In order to achieve such goals, numerous experiments have been conducted. The testing of automotive engine filters is governed by the Society of Automotive Engineers' (SAE) J726 Air Cleaner Test Code (1987). The present study has generally followed the test code.

Automotive air filters commonly consist of a non-woven, cellulose (paper) fibrous mat that is pleated and mounted in either a circular end-seal to form a cylindrical filter, or a single rectangular end-seal to form a panel filter. The panel air filters have been studied extensively in our research program (Sabnis, 1994a, b; Newman, 1994, Duran, 1995) in following the recommendation of the SAE J726 Air Cleaner Test Code. For all filter configurations, it is highly desirable that these filters have high dust-holding capacity, high filtration efficiency and a long life span.

Automotive engine and cabin air filters generally are mounted in housings that are designed to fit within geometrically restricted locations. Consequently, the flow that reaches the filter often has followed a contorted path, and most commonly, approaches the

upstream face of the filter with a high degree of non-uniformity in velocity distribution. The performance of these filters often is measured in test housings such as the universal panel filter test housing recommended by the SAE J726 Air Cleaner Test Code. Test housings likewise may provide the filter with a non-uniform inlet velocity distribution, as previous studies (Sabnis, 1994a, b; Newman 1994; Duran 1995) have documented. The filtration studies conducted by Sabnis (1994a, b) and Newman (1994) have shown that the difference between the non-uniform velocity distribution presented to a filter under test in the universal panel filter housing and the uniform distribution assumed in filter design may result in non-negligible differences between predicted and measured initial filter efficiency.

The main themes of the present study are two-fold: first, through experiments to see how the dust loading capacity responds to increases in the terminating pressure drop. The **terminating pressure drop** Δp is defined as the additional pressure drop beyond the pressure drop measured for the clean filter with the same volumetric flow rate. The dust holding capacity is referred as the amount of dust held inside a filter at a given Δp . During automotive engine operation, with the accumulation of dust on an air filter, the pressure drop across the air induction system must increase in order to maintain the same air supply to the engine. In experiments, the terminating pressure drops are artificially designed to be 50%, 100% 150% and 200% of the full design terminating pressure drop to estimate the relationship between dust loading capacity and the corresponding terminating pressure drop. More intermediate terminating pressure drops may be used in order to obtain a better understanding how the dust capacity responds to the terminating pressure drop.

The second theme of this study is to demonstrate the effects of the dust loading on velocity distributions. From the theories of fluid flow in porous media (the filter paper or the whole filter may be considered as a porous medium), dust loading on a filter decreases the permeability of the filter and increases resistance to fluid flow, and consequently alters the flow field. However, dust distribution on an air filter is not well-known at this stage. It is anticipated that more dust is deposited at the central area of the filter. Liang et al., (1994) conducted a series of filtration efficiency experiments under the SAE J726 and modified J1669 test housings. Their results showed that high particle concentration occurs at the low velocity areas. Liang et al. also showed that the magnitude of axial velocities at the central area can be 6 times higher than those at the edge areas of the filter, while the particle concentration at the central area is, at maximum, 4 times lower than the edge areas of the filter. Therefore, it is anticipated that the dust loading per unit area at the central area of the filter should be as much as 50% more than that at the edge areas.

The experimental procedure of the present study consists of two parts. The first is dust loading on clean filters to prepare dirty filters for the LDA velocity measurement which is the second part of the experiment. With regard to the dust-loading experiments and LDA velocity measurement of the flow field several studies have been conducted by previous students on this project (Liang et al., 1994; Newman, 1994; Sabnis, 1994a, b; Duran, 1995). The present study is based on the work conducted by Newman (1994) and Sabnis (1994a, b) who carried out a series of LDA velocity experiments for clean panel air filters. The configuration of the experimental housing used by Newman, Sabnis and in this study is illustrated in Figure 3.1 and filter characteristics are listed in Table 3.1. The axial

velocity distribution from Newman’s experiment showed that the velocity profile at the center of the clean filter looks like that from a jet flow. The velocity decreases dramatically from the center toward the edges. Flow visualization experiments conducted by Newman (1994), Sabnis (1994a), and Duran (1995) also demonstrated the very non-uniform nature of the velocity field. Furthermore, separation and circulation near the wall were also observed. In the present study, as far as LDA velocity measurements are concerned, only the area directly above the filter is considered. The circulation and separation near the wall areas are neglected.

DESCRIPTION	FILTER AF3192*
Length of filter (m)	0.193
Width of filter (m)	0.121
Height of filter pleat (m)	0.030
Pitch of pleat (m)	0.003125
Design flow rate (m ³ /s)	0.0590
Design uniform velocity outside pleat (m/s)	2.5269

Table 3.1. Filter specifications and design flow rate.

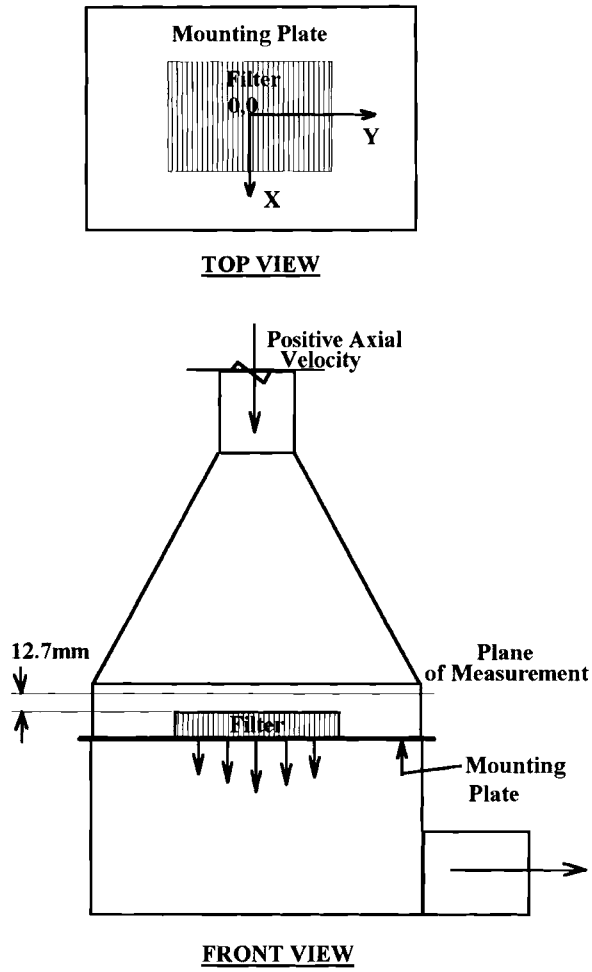


Figure 3.1. A sketch of test housing

3.2 DUST-LOADING EXPERIMENTS

The experiments were conducted using a standard production engine air filter (AF3192), as described in Table 3.1. The dust-loaded dirty filters were prepared following the recommendations of the SAE J726 Air Filter Test Code. All tests were performed at a constant volumetric flow rate of $0.059 \text{ m}^3/\text{s}$ ($125 \text{ ft}^3/\text{min}$) corresponding to the design flow rate of the filter. The volumetric flow rate was measured with an inline Meriam Model 50MR2-6S Laminar Flow Element connected to a temperature and barometric pressure compensated manometer.

The flow was drawn through the system by a Hoffman Model 4207A Centrifugal Exhauster driven by an Allis Chalmers Model 511 29.8 kW (40 hp) electric motor. Clean filters were mounted in the steel test housing and the initial clean filter pressure drop across the housing was measured. The dust injector then was placed in operation, drawing "SAE Fine" test dust from a rotating circular feed tray. The filter loading was stopped when the pressure drop across the housing had increased the desired amount above the initial clean filter value. The pressure drop was measured with a Meriam vertical reservoir manometer. Filters were loaded to capacities corresponding to additional pressure drops of 0.127, 0.254, 0.381 and 0.504 m of water (5, 10, 15, and 20 inches of water). The pressure drop for clean filters is about 36.8 mm (1.45 inch) of water. When the desired pressure increases were achieved, the filters were carefully removed from the steel housing and weighed to determine the amount of dust collected. The filters then were ready for use in the velocity distribution measurement experiments.

Figure 3.2 and Table 3.2 demonstrate that the corresponding capacities and the terminating pressure drops have a nearly linear relationship within the range considered. The relationship may not be linear outside the ranges considered in this study. The filtration efficiency is almost not affected by the increase of the pressure drop. It should be mentioned that the efficiencies obtained in these experiments are relatively low. In automotive air filters, the efficiency is expected to be higher than 99%.

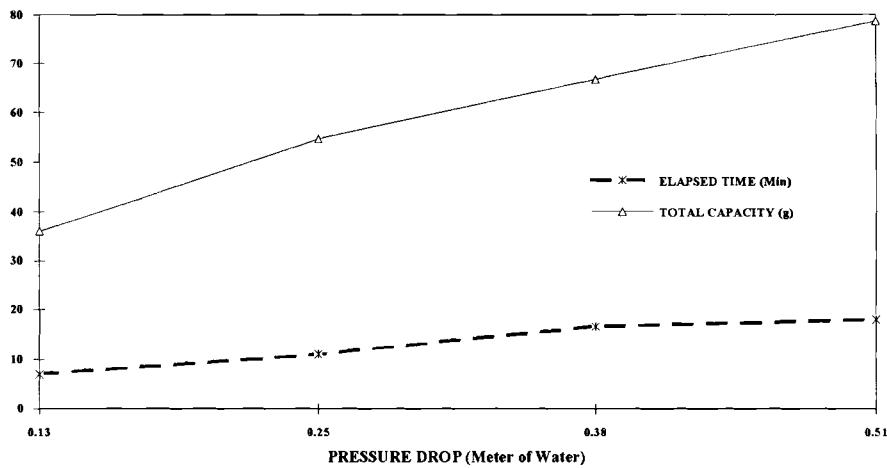


Figure 3.2 The capacities and elapsed dust loading times for various desired additional pressure drops. The flow and other parameters are listed in Table 3.1. The dimensions of the y-axis are grams and minutes for the capacity and elapsed time curves, respectively.

Pres. Drop (m)	Elapsed Time (min)	Capacity (g)	Efficiency
0.127	7.0	36.1	97.4
0.254	11.0	54.7	98.0
0.381	16.6	66.3	98.2
0.508	18.0	78.8	98.1

Table 3.2 The filter capacity and elapsed loading time for various terminating pressure drops.

3.3 LDA VELOCITY MEASUREMENTS

The filters were mounted in the universal panel filter test housing constructed following the recommendations of the SAE J726 Air Cleaner Test Code and illustrated in schematic form in Figure 3.1. The rectangular cross section housing diverges in two planes, giving the appearance of a wide-angled diffuser. The filter under test is mounted in a plate blocking the exit of the diverging section of the housing. A steel test housing was used when the filter was loaded with dust in preparation for the LDA velocity measurements. The LDA velocity measurements were performed with the filter mounted in a duplicate housing constructed of transparent plexiglas and glass. The plexiglas housing allowed optical access for the LDA to focus its beams at the point of the velocity measurements and collect the light scattered by particles passing through the focal point sampling volume.

For the velocity measurements, a filter loaded with dust in the steel test housing was removed, weighed and carefully remounted in the transparent plexiglas housing. This housing was connected to the same flow system as used for the filter loading, so the housing pressure drop and volumetric flow rate could be measured in the same way. It was observed that the pressure drop did display variation during the course of long velocity measurement runs which can last as long as 10 to 15 hours. The maximum variations were approximately 75 to 125 mm water, and these occurred for the highest pressure drop cases. However, checks of filter weight after runs were completed showed that there was very little change in the weight of the filter from the beginning to the end of

the test, either through reentrainment and loss of the original dust particles loaded on the filter, or through LDA seed particle collection during the measurements. The weight of the seed particles presented to the filter during the course of a velocity measurement run may be shown to be negligible. The variations in pressure drop might be attributed to rearrangement of the dust already present in the filter.

The LDA system used for the velocity measurements was an Aerometrics, Inc. 2-component fiber optic system with a Doppler Signal Analyzer processing Doppler bursts in the frequency domain using Fast Fourier Transforms. The instrument is hosted by a 486DX2-66 MHz personal computer. The laser beam is provided by a Coherent Innova 70-A 4 watt argon ion laser. The system fiber drive splits the laser beam into two blue and two green beams. A Bragg cell applies a 40 MHz frequency shift to one beam of each color, enabling determination of flow direction in reversing flow regions.

The four beams are transmitted to the transceiver head through individual fiber optic cables. The transceiver focuses the system's four beams at a 500 mm focal point, producing a probe volume that is 737 μm long and 66 μm in diameter. The transceiver, operating in the back-scatter mode, collects light reflected from seed particles passing through the probe volume. The collected light is transmitted through a fifth fiber optic cable to two photomultipliers, one sensing the signal from the green beams and the other sensing the blue.

The scattered light signal, called the Doppler burst signal, contains intensity maximas and minimas that result from the seed particles crossing the brighter and darker

bands of the interference fringe pattern of the beam intersection. The amplitude of the scattered light thus is modulated at the Doppler frequency. The photomultipliers convert the light to analog voltage signals. With suitable choices of processing parameters, the LDA's signal analyzer detects the Doppler bursts of seeding particles passing through the probe volume and performs a Fast Fourier Transform (FFT) of the digitized burst signal. The peak frequency in the spectrum resulting from the FFT may be considered to be the rate at which the particle is crossing the interference fringes in the probe volume. With the fringe spacing known from the LDA's optical parameters, the velocity of the particle, and hence the fluid, is obtained directly. The LDA processor performs validation tests on the individual spectra, rejecting low quality, noisy data.

The flow was seeded with 1 μm diameter polystyrene latex particles produced from a water solution by an aerosol generator. The seed particles were introduced to the inlet flow upstream of the entrance pipe connecting to the test housing. Care was taken to insure that the water droplets evaporated before reaching the test housing.

The four laser beams of the LDA were aligned so that measurements were performed of the axial velocity component normal to the plane of the filter and the transverse velocity component in the direction of the long axis of the filter. The transceiver head was mounted on a three-axis traversing table with motion in the horizontal plane provided by stepping motors under computer control.

The non-uniform test housing flow required the signal processing parameters of the LDA to be adjusted as the sampling volume was traversed to different points in the

flow field. The different mean velocities, flow directions and seed particle concentrations all contributed to the need to change parameters during the traverse. These variations resulted in data rates and validation rates that were different in different regions of the flow field. In order to provide consistent velocity measurements across the flow field, all measurements reported here resulted from the average of 500 validated samples. This number of validations was easily and rapidly achieved in the central core of the flow. In the slower, more lightly seeded flow away from the centerline, a much longer total time was required to obtain the 500 samples. No corrections were applied for the various biases that may enter into the LDA measurements in the varied flow regions.

The measurements reported here were performed in the plane approximately 12.7 mm (0.5 in) upstream of the filter pleat peaks, as illustrated in Figure 1. The measurement grid was spaced at increments of 12.7 mm (0.5 in) across the short axis (X-axis in figures) of the filter and 25.4 mm (1 in) along the long axis (Y-axis in figures). Measurements were performed on only one half of the plane above the filter, the region corresponding to positive X-coordinates. The measurement region was restricted to enable the measurement plane to be as close to the filter as possible. The minimum measurement height above the filter is dictated by the requirement for the lowest entering laser beam to clear the edge of the filter on its way from the transceiver to the focal point.

3.4 RESULTS AND DISCUSSION

Axial velocity distributions for the clean filter, the filter loaded to capacities corresponding to the terminating pressures of 0.127, 0.254, and 0.381 m of water are presented in Figures 3.3 3.4 and 3.5, respectively. The LDA velocity measurements were performed only for one half plane 12.7 mm directly upstream of the top surface of the filter, and did not include measurements in the recirculating flow to the sides of the filter, upstream of the solid filter mounting plate. The velocity distribution upstream of the clean filter, presented in Figure 3.3, displays a very peaked profile, with high velocities near the center of the filter abruptly falling off to much lower velocities away from the center, near the corners. This impinging jet-like profile is very similar to previous measurements performed for this configuration (Sabnis et al. 1994a, b; Newman, 1995). These measurements show that the universal panel filter test housing does present the filter under test with very non-uniform velocity profiles, unlike the uniform conditions assumed by the filter designer.

The velocity distribution upstream of the half and full designed Δp filters (loaded to terminating pressures of 0.127 and 0.254 m water) are depicted in Figures 3.4 and 3.5, respectively. Comparing with the clean filter axial velocity distribution of Figure 3.3, it may be observed that the maximum velocity at the axial centerline of the filter is reduced and the center of the velocity profile appears somewhat flattened and leveled, in particular for the filter with full design capacity (additional pressure drop of 0.254 m of water). The velocities near the corners of the filter have increased very small amounts above those of

the clean filter. These changes are not so dramatic as might have been expected. The profiles show that this filter is subjected to a very non-uniform inlet velocity profile throughout its capacity test.

Somewhat more dramatic changes in the velocity distribution are evident in the measurements for the filter loaded to a point at which the additional pressure drop is fifty percent greater than the design capacity value. The mass of dust loading for this filter was approximately twenty-three percent greater than that of the design capacity filter of Figure 3.5. The measurements of the axial velocities for this filter are presented in Figure 3.6. It may be observed that the profile, while domed and non-uniform, has been flattened substantially. However, the velocities at the corners of the filter are still only about one quarter of the velocities at the centerline. Thus, even at additional pressure drops fifty per cent greater than design values, the filter still is experiencing significantly non-uniform inlet flow.

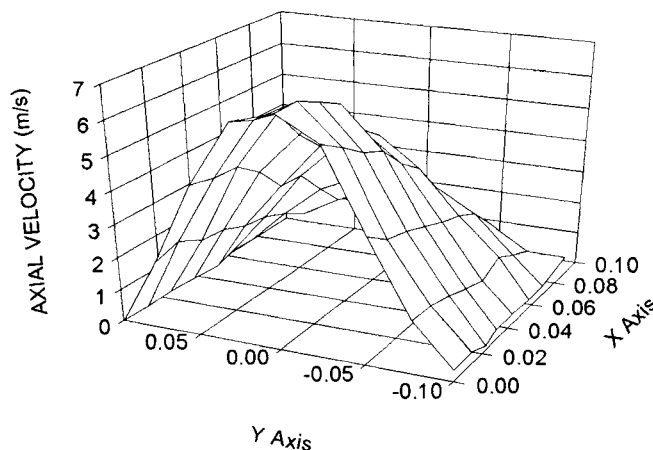


Figure 3.3 The velocity distribution at the plane 12.7 mm upstream of a clean filter with a volumetric air flow rate of $0.059 \text{ m}^3/\text{s}$.

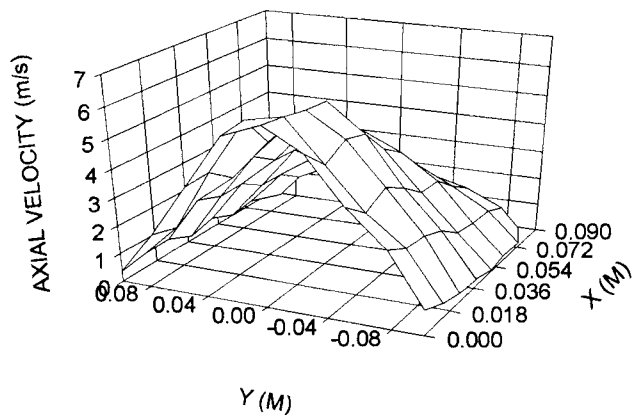


Figure 3.4 The velocity distribution at the plane 12.7 mm upstream of a dirty filter loaded to an additional 127 mm water pressure drop with $0.059 \text{ m}^3/\text{s}$ volumetric air flow rate.

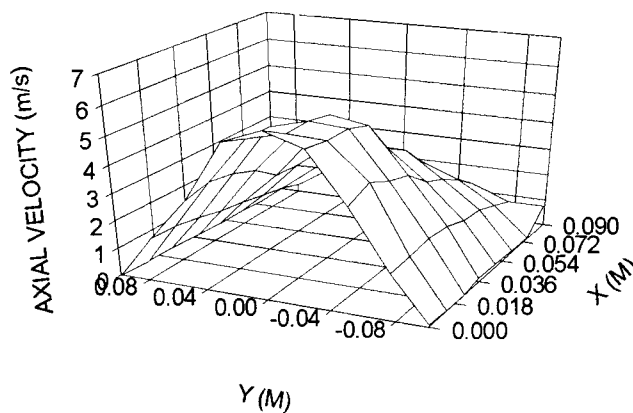


Figure 3.5 The velocity distribution at the plane 12.7 mm upstream of a dirty filter loaded to an additional 254 mm water pressure drop with $0.059 \text{ m}^3/\text{s}$ volumetric air flow rate.

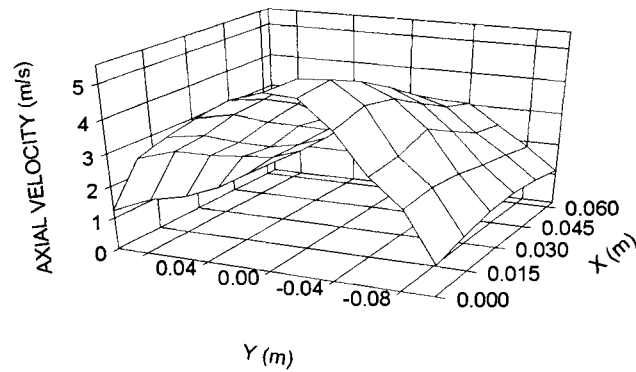


Figure 3.6 The velocity distribution at the plane 12.7 mm upstream of a dirty filter loaded to an additional 381 mm water pressure drop with $0.059 \text{ m}^3/\text{s}$ volumetric air flow rate.

In order to show the effect of dust loading on the axial velocity distribution in detail, a comparison is illustrated in Figure 3.7 for the axial velocities at y equal to zero for the dirty filters of terminating pressure drops of 0.127, 0.254 and 0.381 m of water. From Figure 3.7, we observe that as the dust loading in the filter increases, the velocity profile at the center of the filter tends to flatten. The detailed physics behind such a tendency toward a more uniform velocity distribution is still not certain. It is probably caused by the preferential deposition of dust near the center area of the air filter (Liang et al., 1994). Thus, the resistance to air flow at the center will be higher. Consequently, the very non-uniform inlet flow will diverge as it approaches the filter. The CFD modeling results from Chapter 2 of this thesis show similar trends. They show that if the permeability of the filter at the central area is lower than other areas, the flow will diverge and the velocity profiles upstream of the filter will be flattened.

The transverse velocity profiles from all cases in this study show common characteristics as illustrated in the Figure 3.8. It should be noted that the transverse velocities at the opposite side of the center of the filter have opposite directions, because of the divergent nature near the top surface of the filter. Therefore, the velocities at the opposite sides of the center will have opposite signs as illustrated in Figure 3.8. It seems that the transverse velocity distribution at the level 12.7 mm above the filter is approximately symmetrical. The minimum value occurs at the center of the filter and the maximum occurs at approximately the central area of each side of the center of the filter.

The transverse velocity profiles obtained in this study have almost the same characteristics as those in Newman's (1994) and Sabnis and co-workers' (1994a) experiments. The maximum transverse velocity from the dirty filter with 0.381 m of additional pressure drop is about 0.5 m/s higher than that from the clean filter. This is because the higher the dust loading capacity, the higher the resistance of the filter to the fluid flow. The divergence of the flow upstream of the filter with high dust loading capacity tends to be stronger than that with low dust capacity.

It should be remembered that these velocity measurements were performed in the plane 12.7 mm upstream of the filter and thus are not completely representative of the flow entering the filter. The flow had a short distance in which it could perform further adjustments to the spatial variations in the resistance of the filter, but such final changes in the velocity distribution are believed to be small.

These experiments were conducted for a single production engine air filter. Qualitatively, the observed results may be expected to apply to other filters tested in the universal panel filter test housing. However, the non-uniformity of the flow distribution presented to the filter depends in part upon the extent to which the filter fills the exit of the housing. Previous measurements (Sabnis et al., 1994a, b) for two different size filters have shown that for the clean filter case the larger filter has a more non-uniform velocity distribution. The larger filter had a greater relative area operating at very low velocities. Thus, the magnitude of the velocity redistribution that results from dust loading may be expected to exhibit a dependence upon the filter size.

The results of these experiments also have implications for the performance of filters installed in vehicle housings. The results suggest that the velocity distributions presented to the filter installed in a vehicle will not change dramatically as the filter accumulates dirt. For filters changed at recommended maintenance intervals, the dust accumulation is unlikely to be sufficient to produce an inlet flow that is considerably more uniform than the flow to the clean filter.

However, this implication may be most relevant only for vehicular housings in which the filter is presented with an impinging inlet flow. For an impinging flow, the inertia of the inlet flow may be expected to work against a turning and redistribution of the flow. For a housing in which the inlet flow is introduced tangent to the upper surface of the filter, all of the flow must turn, and the distribution may be more susceptible to the changes in filter resistance that accompany dust loading. This is a topic that requires further study.

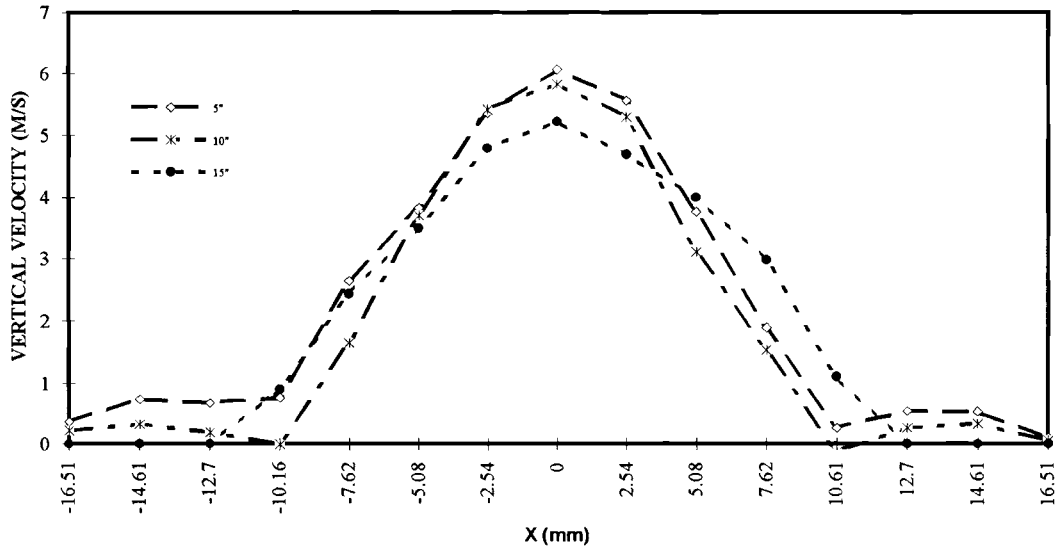


Figure 3.7 A comparison of axial velocity at y equal to zero from dirty filters of terminating pressures of 0.127, 0.254, 0.381 m of water.

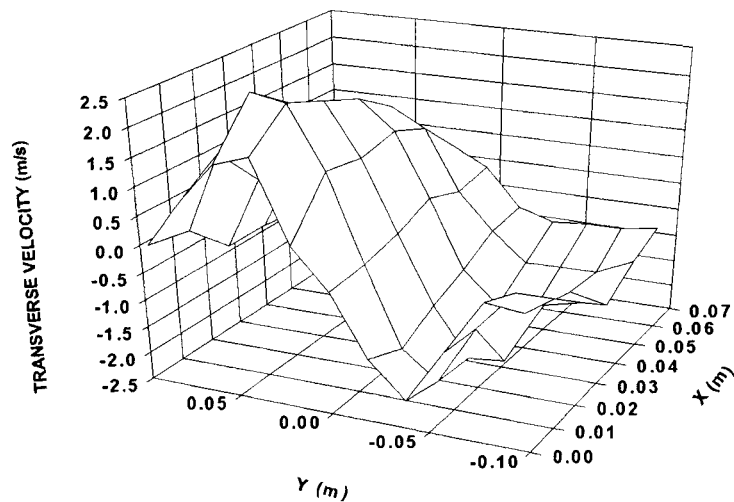


Figure 3.8 The transverse velocity distribution 12.7 mm upstream of a filter loaded to an additional 381 mm water pressure drop with 0.059 m³/s volumetric air flow rate.

3.5 CONCLUSIONS

As the dust loading on an air filter is concerned, the experiments conducted in this study show that there is an approximately linear relationship between the dust loading capacity and the corresponding terminating pressure for Δp ranging from 0.127 to 0.508 m of water. The filtration efficiency is basically independent of the terminating pressure drops at the ranges tested in this study (from 0.127 to 0.508 m of water). However, one should be aware that the experimental data may not be fine enough for the correlation between the dust loading and the terminating pressure drop.

Inlet velocity profile measurements have been conducted for a single production engine air filter mounted in the SAE universal panel filter test housing for different levels of dust loading. For the conditions studied, the following conclusions may be drawn:

- 1.) Dust loading and the accompanying spatial variations in flow resistance across the filter do result in an evening of the velocity distribution approaching the filter. Peak velocities are reduced and the velocity profile is broadened.
- 2.) While velocity distributions are made less peaked and non-uniform, a high degree of uniformity was not achieved for the filter loaded to and substantially beyond design capacity.
- 3.) The qualitative trends observed may be expected to apply to different size filters mounted in the universal panel filter test housing, but size is likely to alter the quantitative changes in the velocity distributions.

4.) Further study is required to determine whether similar changes occur in housings in which the inlet flow does not impinge normally upon the filter.

CHAPTER 4

FUTURE WORK

The quantitative study of the effects of dust deposition on the velocity distribution, the filtration efficiency, and the endurance of automotive air cleaners (filters) is a rapidly advancing subject. It is expected that more achievement will be obtained in the near future. As the author envisions the future development with respect to the measurements and CFD modeling of the flow field inside an automotive air induction system, the following should be investigated further:

First, as far as the LDA velocity measurements are concerned, different planes both upstream and downstream of the automotive air filters should be measured for clean and dirty filters. In doing so, the three-dimensional velocity field of the air induction system can be described. This is of practical significance for the investigation of the uniformity of both the dust deposition and the velocity distribution.

Second, as the CFD modeling is concerned, a three-dimensional computational algorithm should be developed. The algorithm should be able to handle both steady- and unsteady-state fluid flows with the complicated geometry of the computational domain. I strongly recommend that finite element methods be used, instead of finite difference. Finite

strongly recommend that finite element methods be used, instead of finite difference. Finite element methods have incomparable advantages over the finite difference methods in handling the complicated geometry of the computational domain.

Finally, experimental determination of the permeability distribution of a dirty filter. Up to now, there is no document showing the relationship between the magnitude of the dust on a filter and the corresponding permeability of the filter. The permeability is one of the most important factors in the CFD model of the fluid flow in an automotive air induction system. This work, as the author can anticipate, may be carried out in the following way:

- Prepare dirty filters. The step of additional pressure drops between two successive dust loading experiments may be 50.8 mm (2 inches) of water. The additional pressure drop should range from 50.8 (2 inches) to 508 mm (20 inches) of water.
- Conduct LDA velocity measurements. If the available time is very limited, the measurements may be conducted only at the central area of the filter, say 5 points, with 12.7 mm grid space.
- Obtain the average velocity at the center of the filter and then, apply the extended Darcy's law and linear regression to estimate the relationship between permeability and the average axial velocity, and the relationship between the permeability and the dust capacity, and the relationship between the inertial factor and the average velocity.

These estimated relationships can be used to estimate the permeability distribution inside a dirty filter by relationship between the permeability and average velocity. The

LDA velocity measurement may be conducted under the test housing with low angle of the side walls as in Liang and co-workers' study (1994). The housing with low angle side walls (1° to 3°) provides more uniform inlet flow. The more uniform inlet velocity will probably make the effect of the permeability on the velocity redistribution more clear.

REFERENCES

- Brinkman, H.C., 1947, A Calculation of the Viscous Forces Extended by a Flowing Fluid on A Dense Swarm of Particles, *App. Sci. Res. A1*, pp. 27-34.
- Cai, Q., 1993, A Study of Air Filter Flow by Computational Fluid Dynamics, M. S. Thesis, School of Mechanical and Aerospace Engineering, Oklahoma State University, Stillwater, OK, USA.
- Carman, P.C., 1956, *Flow of Gases through Porous Media*, Academic Press, New York.
- Chen, D.R., Pui, D.Y.H., and Liu, B.Y.H., 1993, Numerical Study and Optimization of Pleated Gas Filter, *Proceedings of the 1993 Institute of Environmental Sciences*, pp. 414-422.
- Collins, R.E., 1961, *Flow of Fluids through Porous Material*, Reinhold, New York.
- Commini, G., and Del Giudice, S., 1985, A (k- ϵ) Model of Turbulent Flow, *Numerical Heat Transfer*, Vol. 8, pp. 133-147.
- Darcy, H., 1856, Les Fontains Publiques de La Ville de Dijon, in *Atlas*, Victor Dalmont, Paris, pp. 590-594.
- Duran, R., 1995, Improvement of Flow Uniformity and Modeling of Filtration Efficiencies for Automotive Air Filter Test Housing, M. S. Thesis, School of Mechanical and Aerospace Engineering, Oklahoma State University, Stillwater, OK, USA.
- Gurumoorthy, V., 1990, Computational Fluid Dynamics Modeling of Air Induction System, M. S. Thesis, Dept. of Mechanical Engineering, University of Rhode Island.

- Harlow, F.H., and Welch, J.E., 1965, Numerical Calculation of Time-dependent Viscous Incompressible Flow of Fluid with Free Surface, *The Physics of Fluids*, Vol. 8, No. 12, pp. 2182-2189.
- Hinze, J.O., 1975, *Turbulence*, McGraw Hill, New York.
- Hirt, C.W., Nichols, B.D., and Romero, N.C., 1975, SOLA - A Numerical Solution Algorithm for Transient Fluid Flows, Los Alamos Scientific Laboratory Report LA-5852, April.
- Kays, W.M., and Crawford, M.E., 1993, *Convective Heat and Mass Transfer*, 3rd Edition, McGraw-Hill Inc.
- Lerch, I., and Thomasen, R.O., 1994, *Hydrodynamics of Oil and Gas*, Plenum Press, New York.
- Liang, F., Natarajan, B., Tien, Y., and Dougherty, R. L., 1994, Panel Filter Efficiency Measurements as Applied to Automotive Engine and Cabin Air Filtration, *Proceeding of the 25th Annual Meeting of the Fine Particle Society*, pp. 1-31.
- Lilley, D.G., 1993, *CFD Course Notes*, School of Mechanical and Aerospace Engineering, Oklahoma State University, Stillwater, OK, USA.
- Muskat, M., 1946, *The Flow of Homogeneous Fluids through Porous Media*, Edwards, Michigan.
- Natarajan, B., *Local Efficiency Measurements of Automotive Air Filters Using Laser Doppler Velocimetry*, M. S. Thesis, School of Mechanical and Aerospace Engineering, Oklahoma State University, Stillwater, OK, USA.
- Newman, R.A., 1994, *Uniformity of Air Flow in Automotive Air Filter Test Housing and Its Effects on the Efficiency of Fibrous Filter*, M. S. Thesis, School of Mechanical and Aerospace Engineering, Oklahoma State University, Stillwater, OK, USA.
- Panda, M.N., and Lake, L.W., 1994, Estimation of Single-Phase Permeability from Parameters of Particle Size Distribution, *AAPG Bulletin*, Vol. 78, No 7, pp. 1028-1039.

- Ramaswamy, B., 1990, Efficient Finite Element Method for Two-Dimensional Fluid Flow and Heat Transfer Problems, Numerical Heat Transfer, Part B, Vol. 17, pp 123-154.
- Rodi, W., 1980, Turbulent Model for Environmental Problems, in: Prediction Methods for Turbulent Flows, Hemisphere Publishing Corporation, New York, Wolfgang Kollman (editor), pp. 259-349.
- Rosner, D.E., 1986, Transport Processes in Chemically Reacting Flow Systems, Butterworth Publishers.
- Sabnis, R.D., 1993, Effects of Non-uniformity Air Flow through Filters on Filtration Efficiency, M. S. Thesis, School of Mechanical and Aerospace Engineering, Oklahoma State University, Stillwater, OK, USA.
- Sabnis, R.D., Cai, Q., and Chambers, F.W., 1994a, Diagnosis of the Flow Fields in A Housing for Air Filter Performance Testing, American Institute of Aeronautics and Astronautics Paper AIAA-94-0117.
- Sabnis, R.D., Cai, Q., and Chambers, F. W., 1994b, Flow Distribution Effects upon Air Filter Performance Measurements, SAE SP-1040, *Climate Control and Automotive Cabin Air Filtration*, 1994. Also available as Society of Automotive Engineers Paper 940317.
- Scheidegger, A.E., 1974, Physics of Flow through Porous Media, Academic Press, New York.
- Slider, H.C., 1976, Practical Petroleum Reservoir Engineering Methods, PennWell Books.
- Society of Automotive Engineers, 1987, SAE J726 Air Cleaner Test Code - SAE Recommended Practice, SAE, Inc., Warrendale, Pa.
- Tebbutt, C.B., 1995, CFD Model of Flow through Air Filter Pleats, M.S. Thesis, School of Mechanical and Aerospace Engineering, Oklahoma State University, Stillwater, OK, USA.

Vafai, K., and Tien, C.L., 1981, Boundary and Inertia Effects on Flow and Heat Transfer in Porous Media, *J. Heat Mass Transfer*, Vol. 24, pp. 195-203.

Wilcox, D.C., 1993, *Turbulent Modeling for CFD*, DCW Industries, Inc. La Canada, California.

APPENDIX

X	C1	C2	C3	C4
-16.50	0.285	0.367	0.219	0.000
-14.61	0.740	0.741	0.326	0.000
-12.70	0.592	0.679	0.192	0.000
-10.16	0.271	0.759	-0.006	0.900
-07.62	1.600	2.641	1.651	2.430
-05.08	3.803	3.830	3.701	3.500
-02.54	6.112	5.359	5.413	4.800
00.00	6.769	6.056	5.825	5.220
02.54	6.112	5.556	5.295	4.700
05.08	4.511	3.759	3.113	4.000
07.63	2.049	1.892	1.541	2.980
10.61	-0.187	0.263	-0.138	1.100
12.70	0.254	0.543	0.258	0.000
14.61	0.411	0.531	0.330	0.000
16.51	0.366	0.099	0.054	0.000

Table A.1 The axial velocities at y equal to zero for a clean filter (C1), and dirty filters with terminating pressure drops of 127 mm (C2), 254 mm (C3), 381 mm (C4) water, respectively.

VITA

Guojiang Liu

Candidate for the Degree of

Master of Science

Thesis: VELOCITY MEASUREMENTS AND CFD PREDICTIONS OF FLOW
REDISTRIBUTION THROUGH AIR FILTERS

Major Field: Mechanical Engineering

Biographical:

Personal Data: Born in Hebei, P. R. China on November 19, 1963, the son of Shuqin Liang and Guangsheng Liu.

Education: Received Bachelor of Science Degree in Petroleum Geology from the Petroleum University, Dongying, P. R. China in June 1983 and Philosophy of Science Degree in Petroleum Geology from the Norwegian Institute of Technology, University of Trondheim, Trondheim, Norway in January 1994. Completed the requirements for the Master of Science Degree with major in Mechanical Engineering at Oklahoma State University in December 1995.

Experience: Employed by the Research Institute of Changqing Petroleum, Gansu, P.R. China from 1983 to 1987 as a geologist. From 1988 to the end of 1993, worked on basin modeling for IKU Petroleum Research, Trondheim, Norway.

Professional Membership: none